Structure and Formation of Convection of Secondary Rainbands in a Simulated Typhoon Jangmi (2008)

Jing Xiao, Zhe-Min Tan and Kim-Chiu Chow, 2018

Meteorology and Atmospheric Physics

Speaker: 陳威縉

Advisor: 楊明仁 教授

Date: 3 Jan, 2019

OUTLINE

1. Introduction
2. Overview of super typhoon *Jangmi* (2008)
3. Convective structure of secondary rainbands
4. Formation and evolution of convection in secondary rainbands
5. Discussions
6. Summary

I)
Introduction

Previous Studies

- **Tropical cyclone rainbands (TCRs) (Dvorak, 1975; Willoughby et al., 1984; Guinn and Schubert, 1993; Wang, 2008; Houze, 2010).**
- **3 types of spiral-shaped rainbands out of eyewall(s):**
  Principal rainbands (PRs)
  Secondary rainbands (SRs)
  Distant rainbands (DRs)
  (Willoughby et al., 1984; Willoughby, 1988; Houze, 2010).
- **PRs are generally convective in the upwind to mid-wind sector, and become stratiform-dominated in the downwind sector as the CAPE decreasing (Barnes et al., 1991; Bogner et al., 2000).**

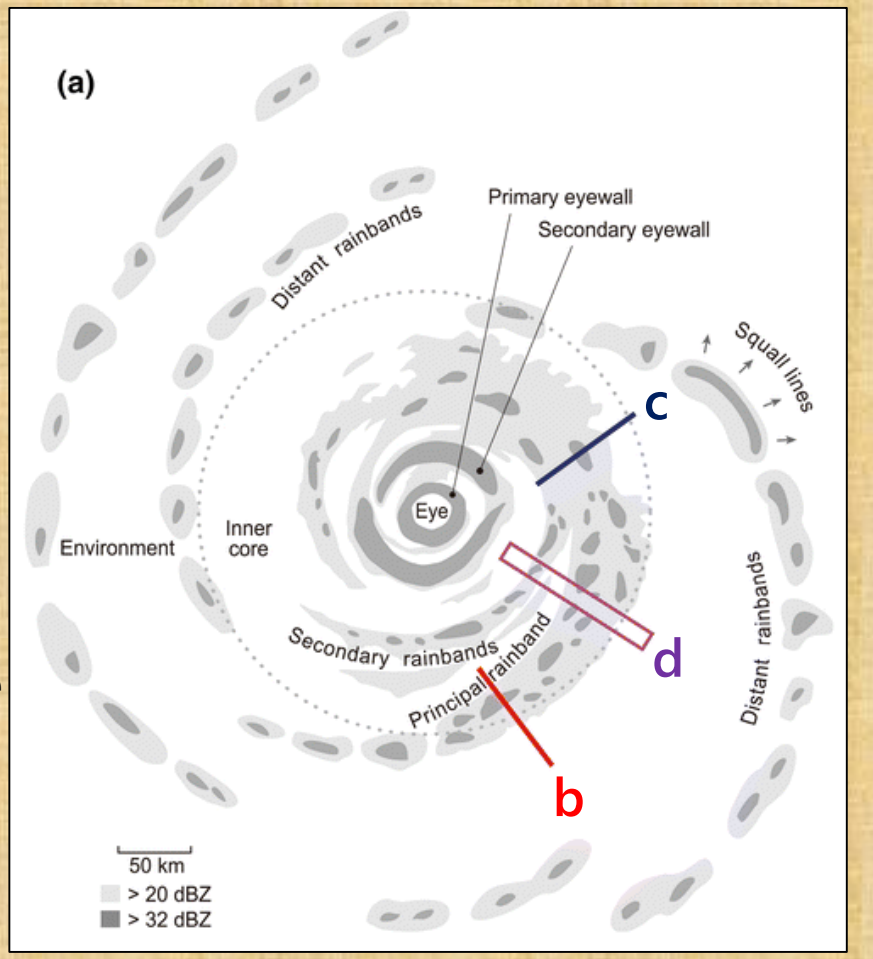

Fig. 1a
Types of rainbands (Houze, 2010).

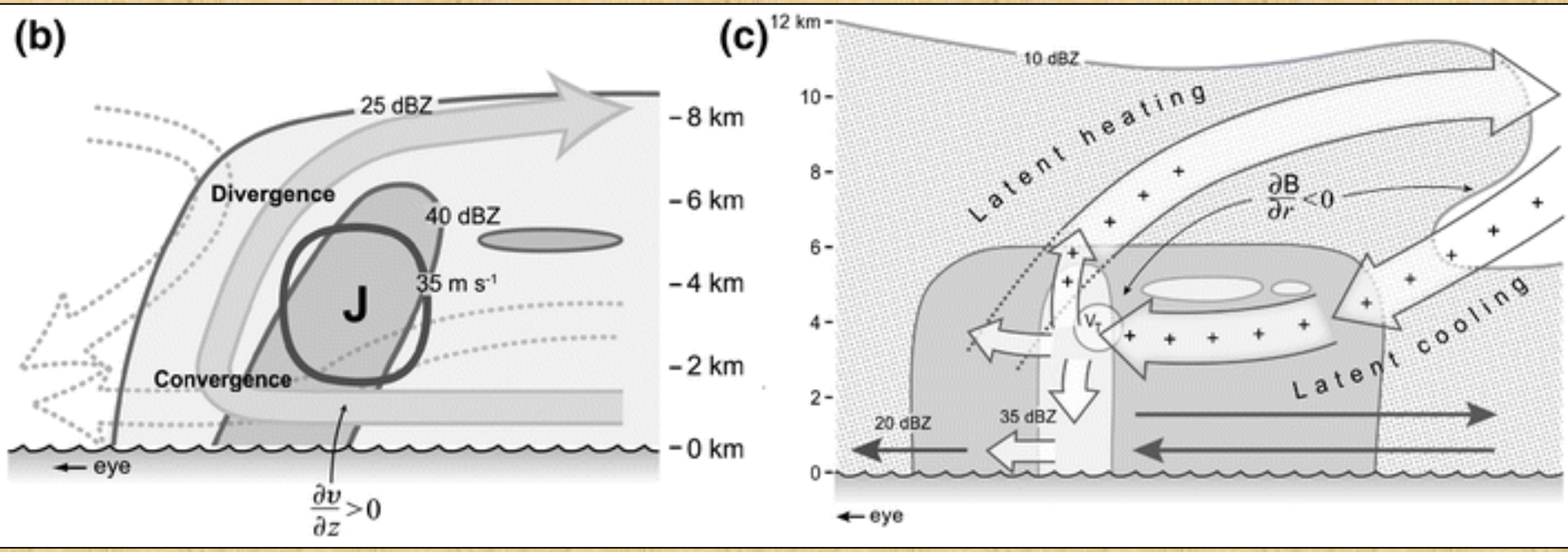

Fig. 1b
PR mid-wind (convective-dominated) sector (Houze, 2010).
Fig. 1c
PR down-wind (stratiform-dominated) sector (Didlake and Houze, 2013b).
The convective structures of the quasi-stationary PRs have been revealed (Barnes et al.,1983, 1991; Powell, 1990a; Houze et al., 2006; Hence and Houze, 2008; Didlake and Houze, 2009, 2011, 2013b; Houze, 2010**).**
Increments of tangential wind (due to the advections of angular momentum) in PRs are related to the formation of secondary eyewalls (Houze et al., 2006; Judt and Chen, 2010; Didlake and Houze, 2013a, b**).**

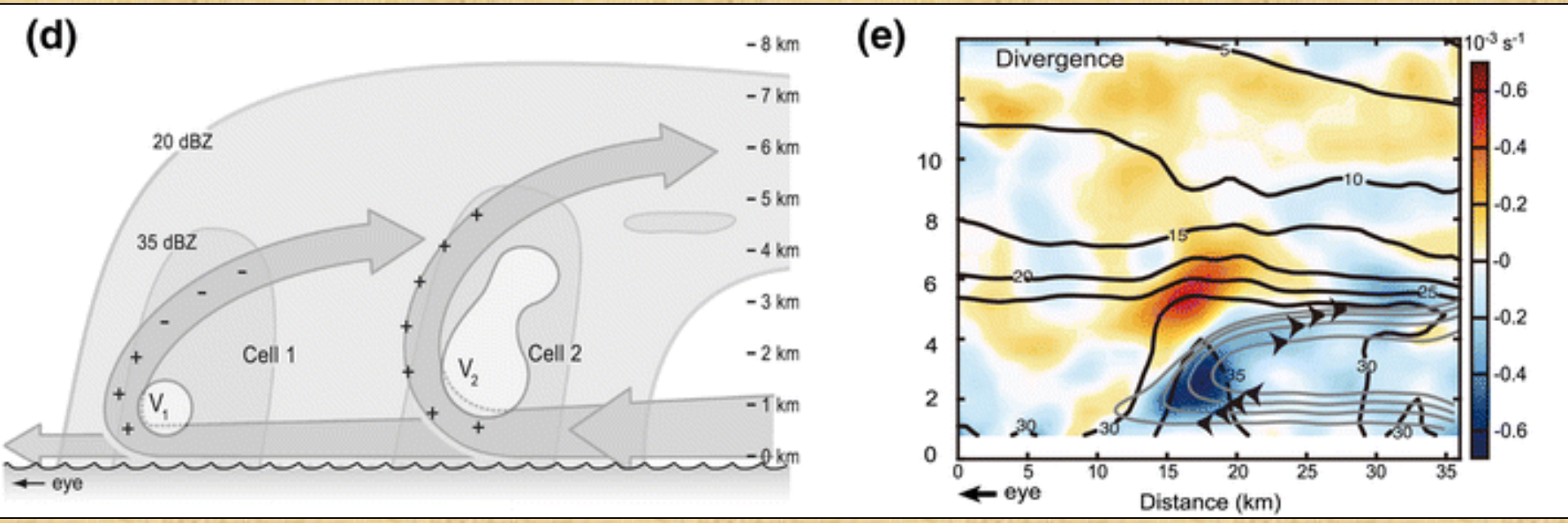

Fig. 1d

Inner core: SR+PR (Didlake and Houze, 2013a).

Fig. 1e

The observed composite structure of convections in one SR (Didlake and Houze, 2013a).

Limited observations of SRs by microwave channels of polar satellites and airborne Doppler radars.

Hurricane Rainband and Intensity Change Experiment (RAINEX, Houze et al., 2006)

Previous Studies

- **TC rainbands can also be classified as inner and outer rainbands based on dynamics (Wang, 2008).**
  SRs belong to inner rainbands, which are located within 3*RMW and their generation is related to vortex Rossby wave (VRW) dynamics (Guinn and Schubert, 1993; Montgomery and Kallenbach, 1997; Reasor et al., 2000; Wang, 2002a).
- **Numerical simulations have revealed some convective structures of the inner rainbands (Chen and Yau, 2001; Wang, 2002a,b; Qiu et al., 2010; Li and Wang, 2012b; Hall et al., 2013; Moon and Nolan, 2015a, b), but are generally different from the usual conceptual model of SRs (Fig. 1d). Therefore, the convective structures of SRs and their relationships with the inner rainbands are still unclear.**

In This Study

1. What is the convective structure of the SRs in a mutual TC?
2. What are the main differences between SRs and PRs?
3. What are the formation and evolution process of SRs?

II)
Overview of Super Typhoon Jangmi (2008)

Overview of Super Typhoon Jangmi (2008)

- *Jangmi* (2008) was a category-5-equivalent typhoon over the west North Pacific.

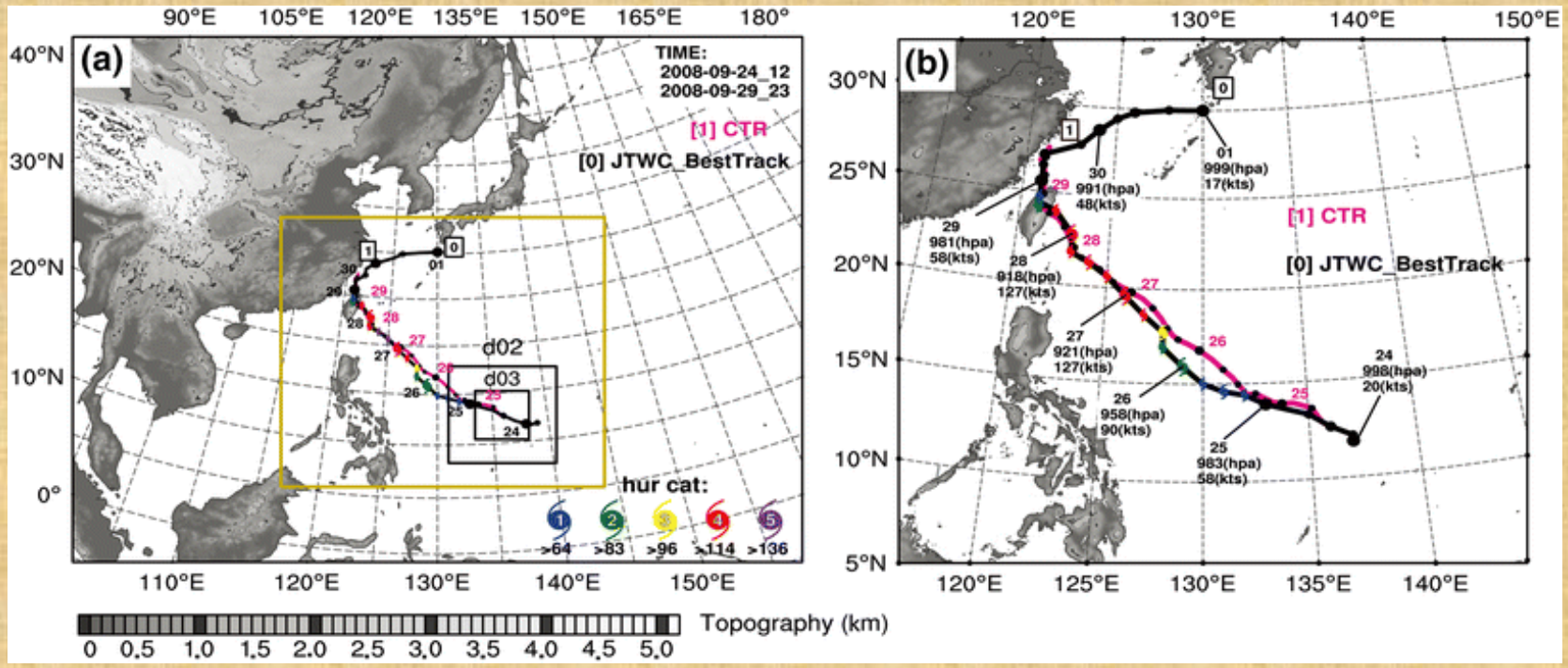

Fig. 2 *Jangmi's* track.

Overview of Super Typhoon Jangmi (2008)

- 91 GHz polarization corrected temperature (PCT) (Spencer et al., 1989), which is most sensitive to large snowflake in deep convections.
- $PCT = \frac{\beta T_{Bh} - T_{Bv}}{\beta - 1}$, $\beta = \frac{T_{Bvc} - T_{Bvo}}{T_{Bhc} - T_{Bho}}$.

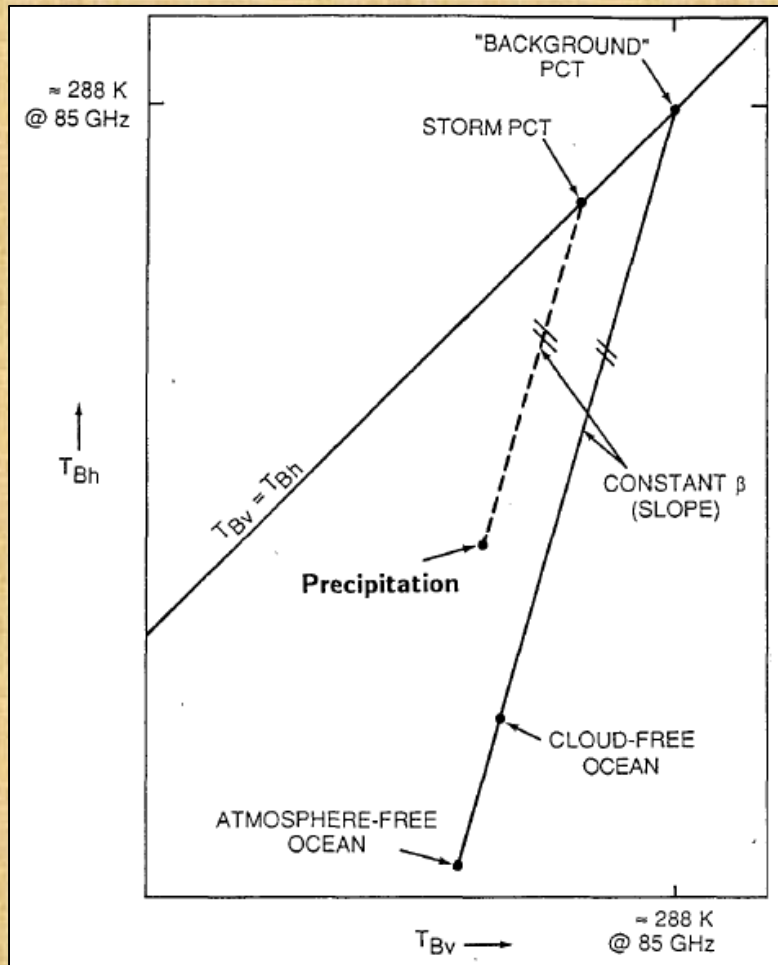

FIG. 5. Conceptual diagram of the relationships between the vertically and horizontally polarized brightness temperatures of the ocean without an overlying atmosphere, with an overlying atmosphere, a hypothetical precipitation observation, the resulting polarization corrected temperature (PCT) of the storm, and the ocean background PCT. See text for explanations of the PCT.

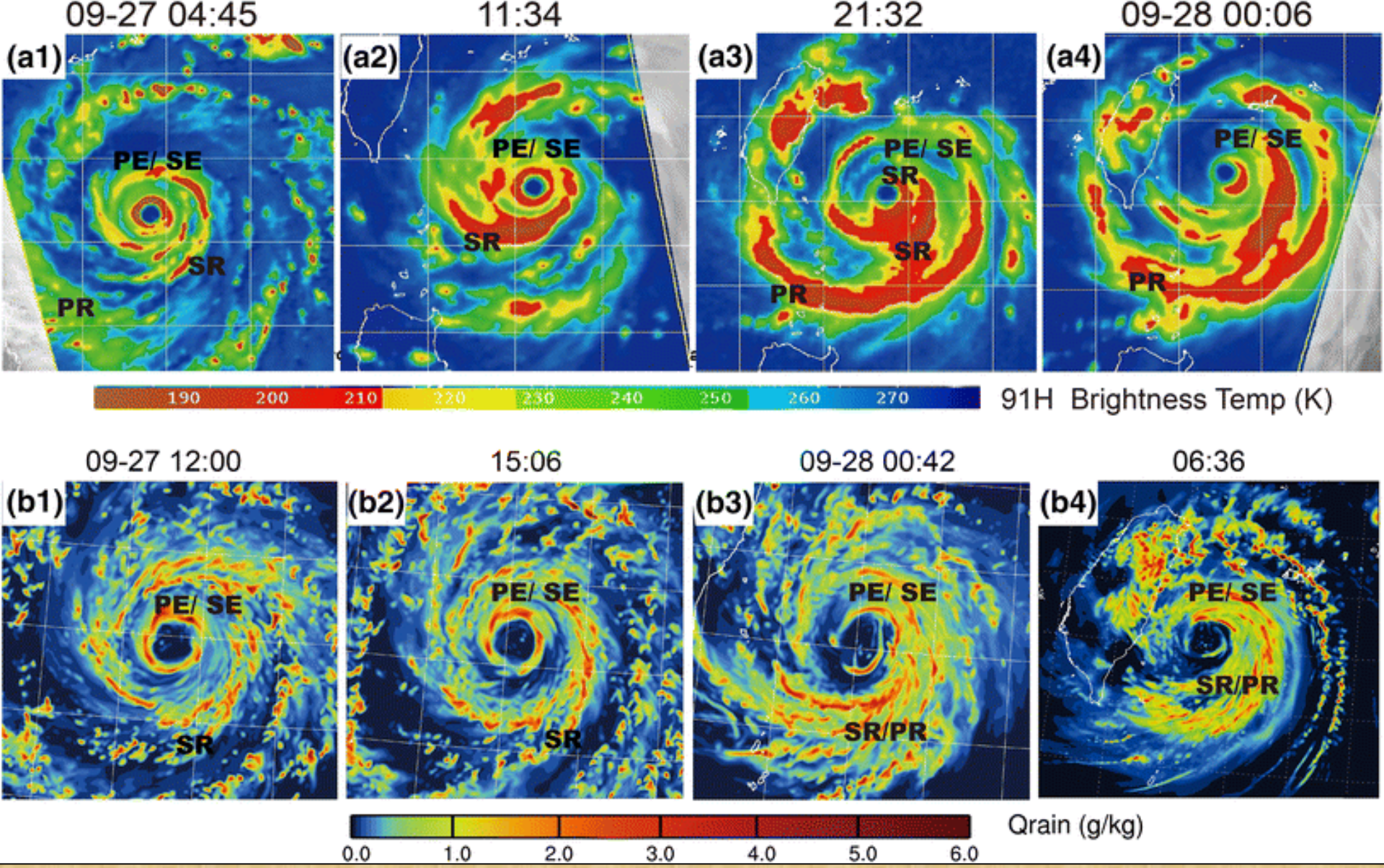

Fig. 5

(a) F16/17 91 GHz PCT images from Navy Research Laboratory (NRL), US;

(b) Simulated surface rain water mixing ratio.

Numerical Model and Experimental Design

- Advanced research Weather Research and Forecasting (WRF) model (Skamarock et al., 2008) ver. 3.1.
- 3 two-way nested domains (D01/2/3).
- Ics and BCs for D01 were provided by the Year of Tropical Cyclone (YOTC) 0.5° reanalysis dataset.
- The results of D03 were output every 6 min to track the evolution of convections.

The detailed configurations are shown in the next page.

WRF Configurations		Domain 1 (D01)	Domain 2 (D02)	Domain 3 (D03)
Domain	-	Fixed	Movable to the vortex	
	Horizontal resolution	15 km	5 km	1.67 km
	Grid points	541 × 435	241 × 241	361 × 361
	Range	8100 × 6510 km	1200 × 1200 km	600 × 600 km
	Vertical level	35 terrain-following and hydrostatic levels		
	Vertical resolution	70 m near the surface to ~1000 m at the model top (50 hPa)		
Scheme	Microphysics	Single-moment 6-class (Dudhia et al., 2008)		
	Cumulus parameterization	Kain-Fritsch (Kain, 2004)	Resolved explicitly	
	PBL	Yonsei University (Hong et al., 2006)		
	LW radiation	Rapid radiative transfer model (RRTM)		
	SW radiation	Dudhia (Dudhia, 1989)		
Time	Simulation time	1200 UTC 24 Sep to 0000 UTC 30 Sep, 2008 (132 h)		
	Time steps	60 s	20 s	6.67 s

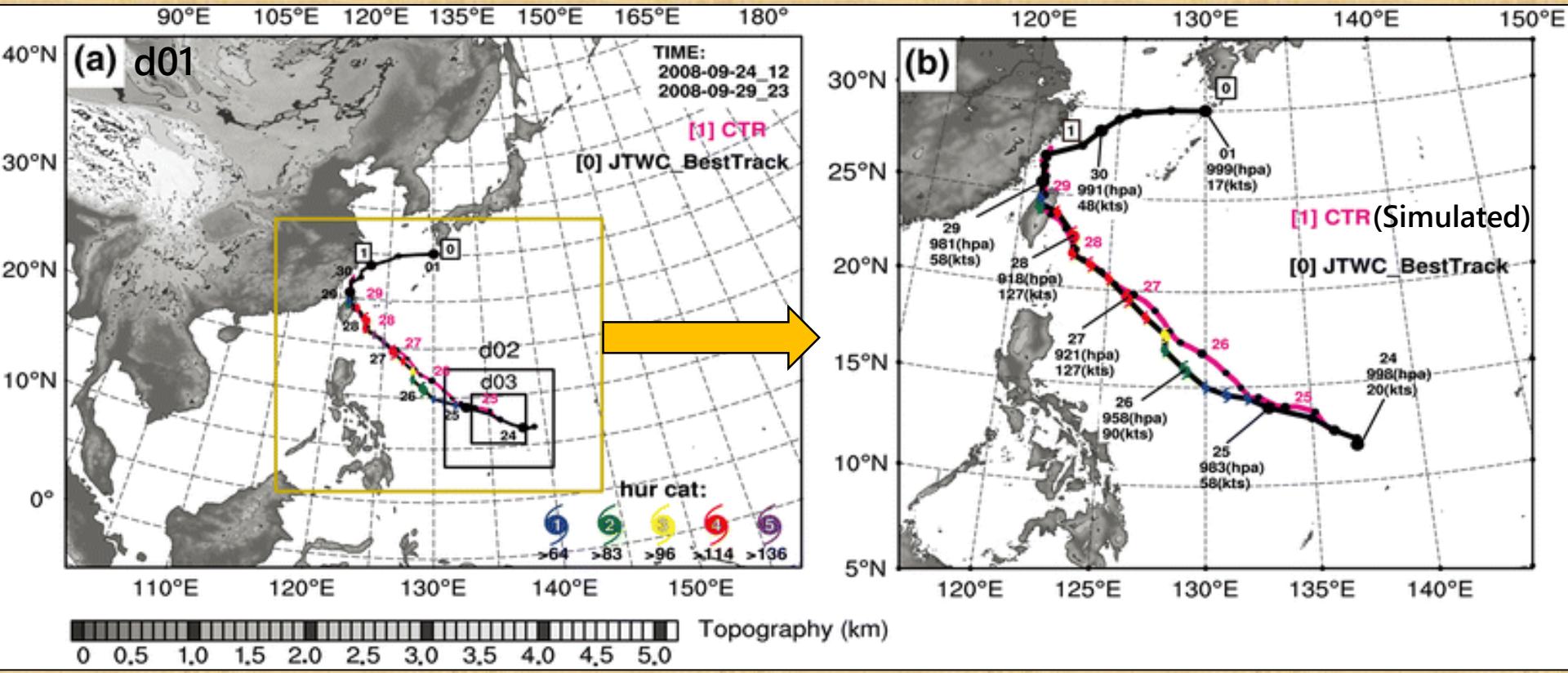

Fig. 2 *Jangmi's* track.

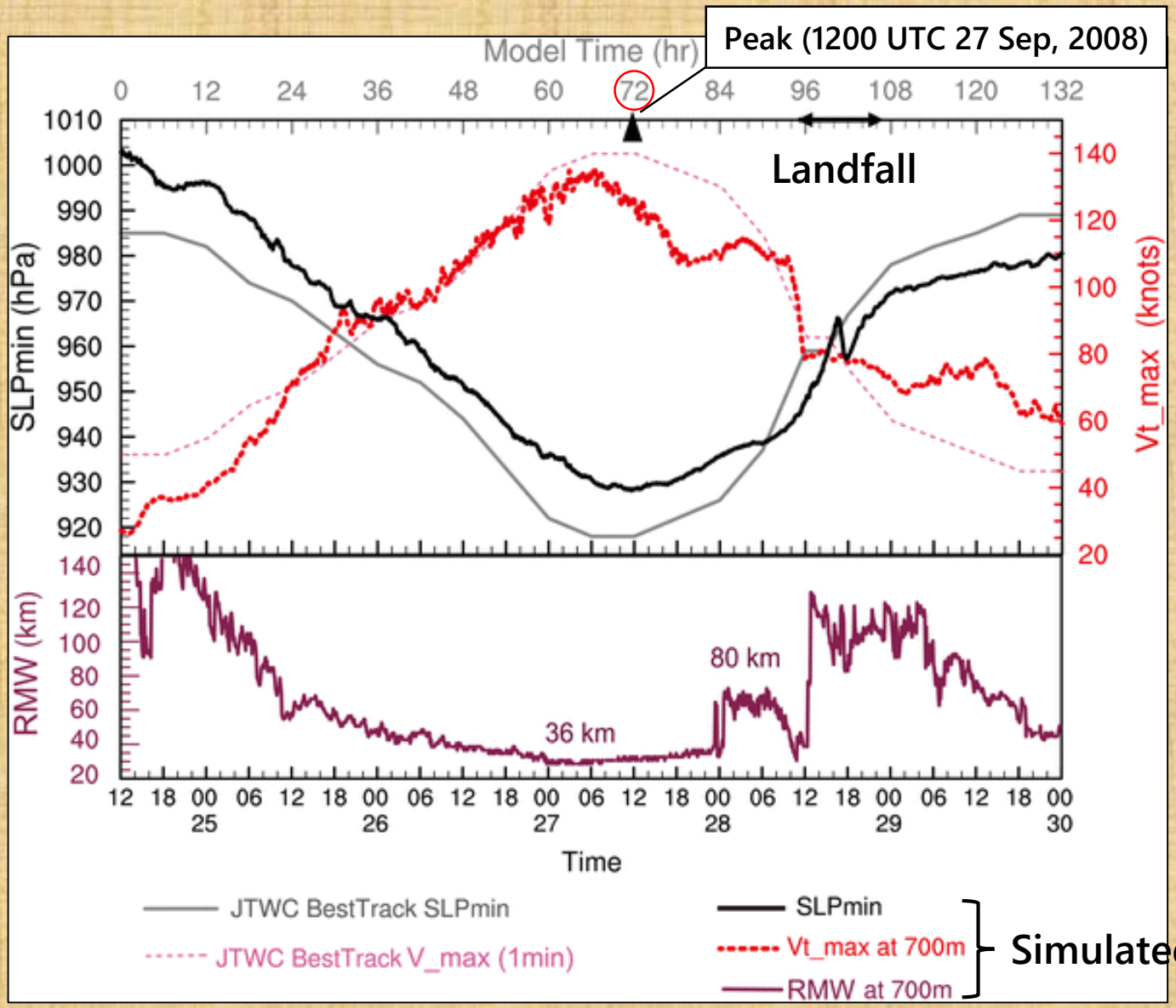

Fig. 3
Evolution with time of the intensity and structure of *Jangmi*.

- **Two convergence regions within the boundary layer (BL) inflow (black arrows) were related with super-gradient force deceleration.**
- **Two shallow outflow centers above the BL (purple arrows) were related with sub-gradient force acceleration (Smith et al., 2009).**
- **Updraft in the SE was weaker and wider.**

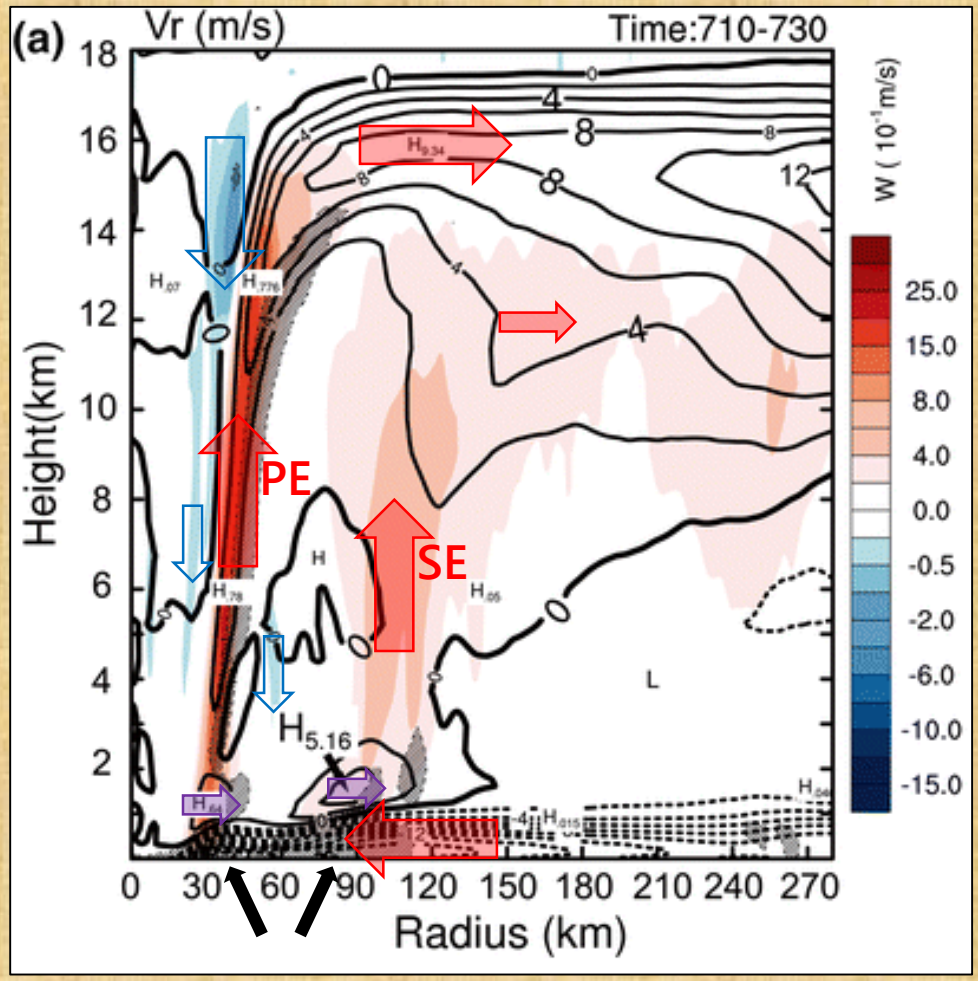

Fig. 4a
Radius-height diagram of azimuthal mean structure (radial & vertical wind).
 # Contour: negative values are dashed;
 # Slash shading: horizontal convergence regions.

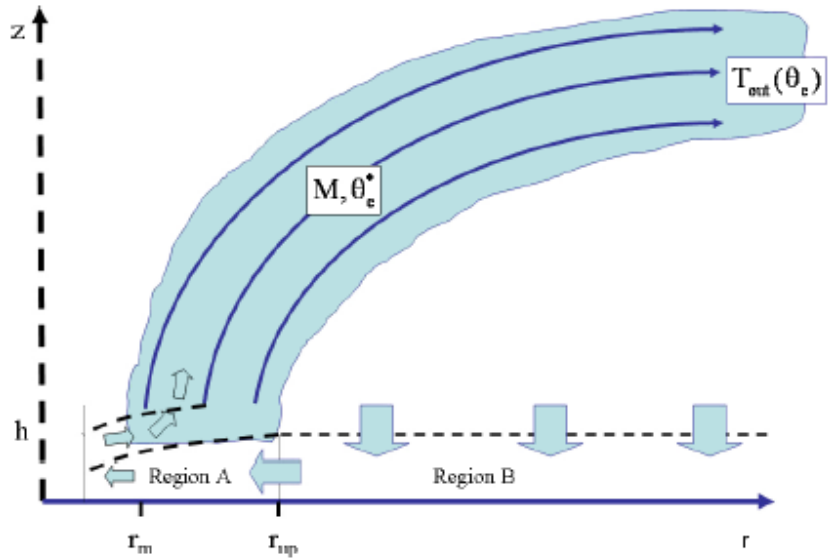

Figure 6. Modified conceptual model of the hurricane inner-core region motivated by the findings herein together with recent observational and modelling studies. Air subsides into the boundary layer for $r > r_{up}$ and ascends out of the boundary layer for $r < r_{up}$. The frictionally induced net inward force in the outer region produces a radially inward jet at $r = r_{up}$. The subsequent evolution of this jet depends on the bulk radial pressure gradient that can be sustained by the mass distribution at the top of the boundary layer. The jet eventually generates supergradient tangential winds whereafter the radial flow rapidly decelerates and turns upwards and outwards. When the outflow has adjusted to the radial pressure gradient that is sustained by the mass field, the flow turns upwards into the eyewall clouds. See sections 5 and 6 for further details. This figure is available in colour online at www.interscience.wiley.com/qj

Smith et al., 2008, **Fig. 6**

Supergradient force deceleration and subgradient force acceleration.

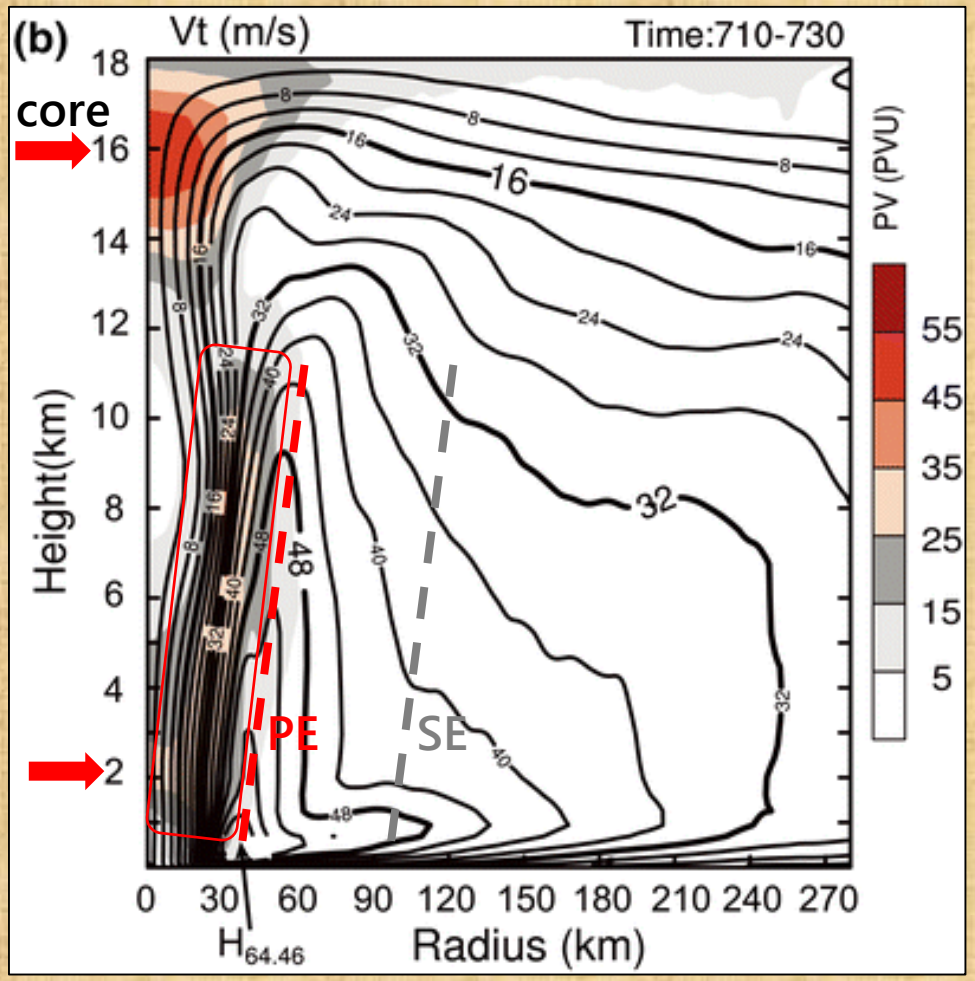

Fig. 4b

Radius-height diagram of azimuthal mean structure (tangential wind & PV).

III)
Convective Structure of Secondary Rainbands

Convective Structure of Secondary Rainbands

- Primary and secondary eyewall (PE and SE).
- Two principal rainbands (PR1 and PR2).
- Two secondary rainbands (SR1 and SR2).
- Two distant rainbands (DR1 and DR2).

Semi-Automatic Rainband Tracking Algorithm

- The rainband axes are determined by the local reflectivity maximum in each radial cross-section.
- Reflectivity field at 2-km height.
- Polar coordinates with resolutions of 1 km (radial) and 0.5° (azimuthal).

The detailed steps are shown in the next page.

1

- Interpolate the reflectivity field into a polar coordinates.
- Origin point at the vertical weighted averaged of the vorticity centroid.

2

- Determine the initial/end positions of the rainbands and the radial searching range artificially.
- Range: from 3–5 km inside to 5–10 km outside the rainband axis.

③

- Iterative calculations are repeated in each cross-section, and the result (rainband axis) will be considered as the first-guess position for the next radial cross-section (cyclonically).

4

- Gap (≤ 40 dBZ) between the convection cells requires extra anchor points (iteration calculation skipped).
- Linear extrapolation from both ends.

Fig. 6
Rainbands in the simulated typhoon *Jangmi* at 1200 UTC 27 Sep, 2008 (t = 72 h).
(a)
Composite reflectivity and axes of eyewalls and rainbands (PRs are separated into downwind, mid-wind and upwind sectors).
(b)
Low-level (below 1 km) averaged horizontal divergence of the moist flux (MFD_h).

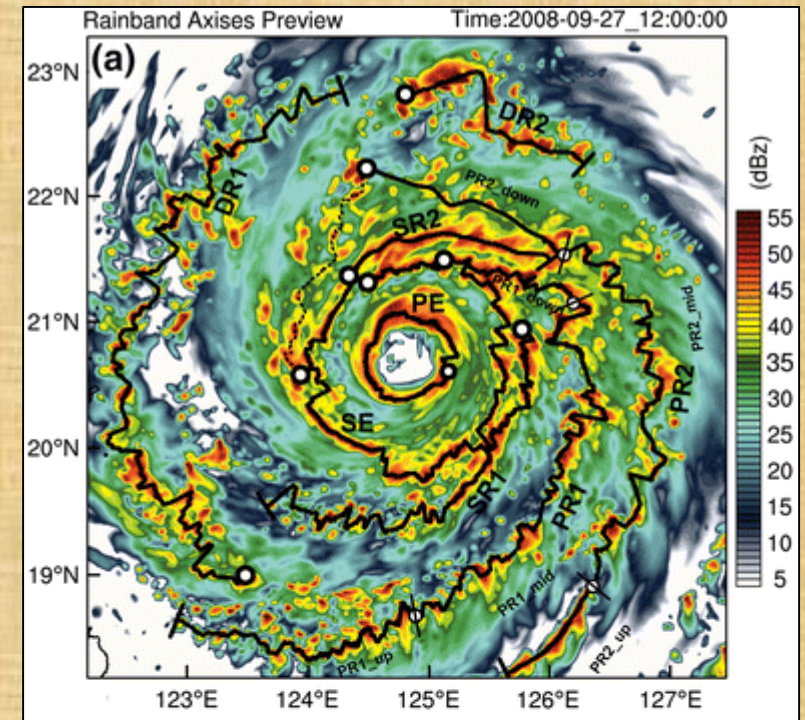

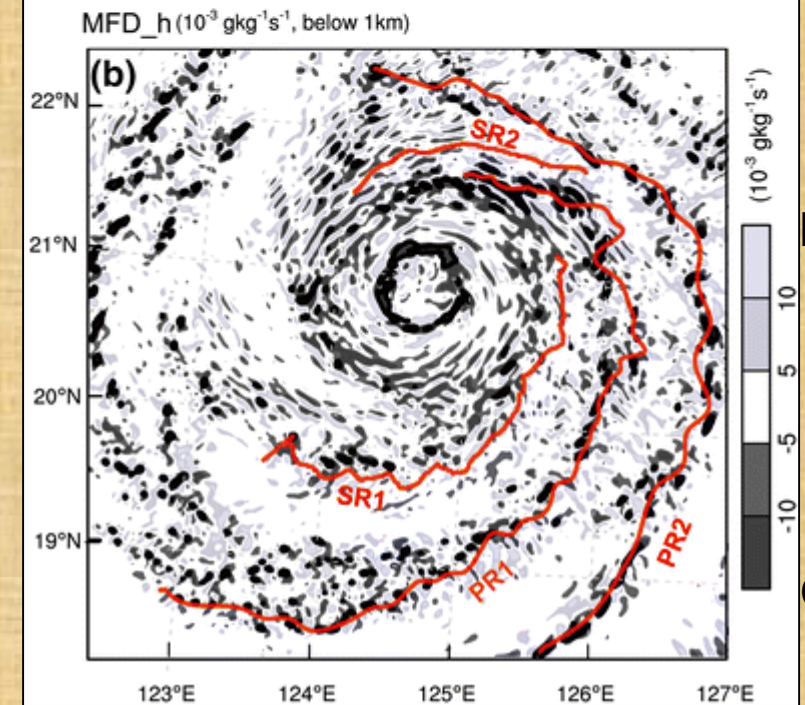

Div.

Conv.

Table 1 Environmental conditions around the rainbands in the simulation of super-typhoon Jangmi

Rainband	Radius (km)	CAPE (J kg^{-1})	MFD_h (10^{-3} g kg^{-1} s^{-1})		$\Delta\theta$ (K)	
			LL	ML	LL	ML
PE	**39.2**	**538**	−5.3	−0.26	6.5	9.9
SE	**94.2**	**846**	−3.1	0.23	2.9	0.5
SR1	137.1	1355	**1.3**	**−3.1**	1.8	3.6
PR1						
Mean	191.6	1248	−8.5	−0.17	1.4	1.2
Down	**101.8**	**771**	−14.9	2.7	3.6	0.7
Middle	187.9	1497	−7.7	−0.63	0.6	1.4
Up	287.8	1785	−6.5	−2.3	0.7	1.7
SR2	116.3	**762**	**0.42**	**−3.0**	1.7	4.8
PR2						
Mean	213.7	1602	−6.5	−0.34	**−0.2**	0.8
Down	159.8	**987**	−6.3	0.80	0.1	1.7
Middle	229.6	1882	−7.4	−1.1	**−0.4**	1.2
Up	297.5	2149	−26.7	−0.85	**−1.7**	**−4.3**
DR1	257.9	1538	−6.7	0.51	**−1.3**	**−1.3**
DR2	242.1	1644	−5.0	−0.10	**−2.4**	**−0.3**

The radius is the mean distance of the rainband from the center of the tropical cyclone; CAPE is the maximum value of convective available potential energy (averaged radially −20 to +30 km to the rainband axis); and MFD_h is the horizontal divergence of the moisture flux (averaged radially ±2 km); LL is the low-level (below 1 km height) average and ML is mid-level (2~5-km height); and $\Delta\theta$ is the difference between the potential temperature outside (averaged radially 5–20 km) and inside (averaged radially −5 to −20 km) the rainband; The Mean, Down, Middle and Up are, respectively, the whole, downwind, midwind and upwind sector of the principle rainband 1 and 2. The separation points are marked out in Fig. 6a

These values in bold mark: 1) radius smaller than 3 RMW; 2) CAPE smaller than 1000 J kg^{-1}; 3) MFD_h <0 (divergence) within boundary layer and >0 (convergence) at mid-levels; 4) inward decreasing of θ from the outer side

Rainband		Radius [km]	CAPE [J kg^{-1}]	MFD_h [10^{-3} g kg^{-1} s^{-1}]		$\Delta\theta$ [K]	
				LL	ML	LL	ML
PE		**39.2**	**538**	-5.3	-0.26	6.5	9.9
SE		**94.2**	**846**	-3.1	0.23	2.9	0.5
SR1		137.1	1355	**1.3**	**-3.1**	1.8	3.6
PR1	Mean	191.6	1248	-8.5	-0.17	1.4	1.2
	Down	**101.8**	**771**	-14.9	2.7	3.6	0.7
	Middle	187.9	1497	-7.7	-0.63	0.6	1.4
	Up	287.8	1785	-6.5	-2.3	0.7	1.7
SR2		116.3	**762**	**0.42**	**-3.0**	1.7	4.8
PR2	Mean	213.7	1602	-6.5	-0.34	**-0.2**	0.8
	Down	159.8	**987**	-6.3	0.80	0.1	1.7
	Middle	229.6	1882	-7.4	-1.1	**-0.4**	1.2
	Up	297.5	2149	-26.7	-0.85	**-1.7**	**-4.3**
DR1		257.9	1538	-6.7	0.51	**-1.3**	**-1.3**
DR2		242.1	1644	-5.0	-0.10	**-2.4**	**-0.3**
Red bold mark		< 3 RMW	< 1000	Div. at LL & Conv. at ML		< 0 (inward)	

Convective Structure of Secondary Rainbands

- SR1 and SR2 were located at about 3*RMW (~114 km), which is beyond horizontal shear-dominated zone and the CAPE~1000 J kg^{-1}.
- The bulk Richardson number (BRN) was less than 50, indicating that it was a favorable condition for long-lived convections (Weisman and Klemp, 1982).
- $R_B = \frac{(g/T_v)\Delta\theta_v\Delta z}{(\Delta U)^2+(\Delta V)^2}$

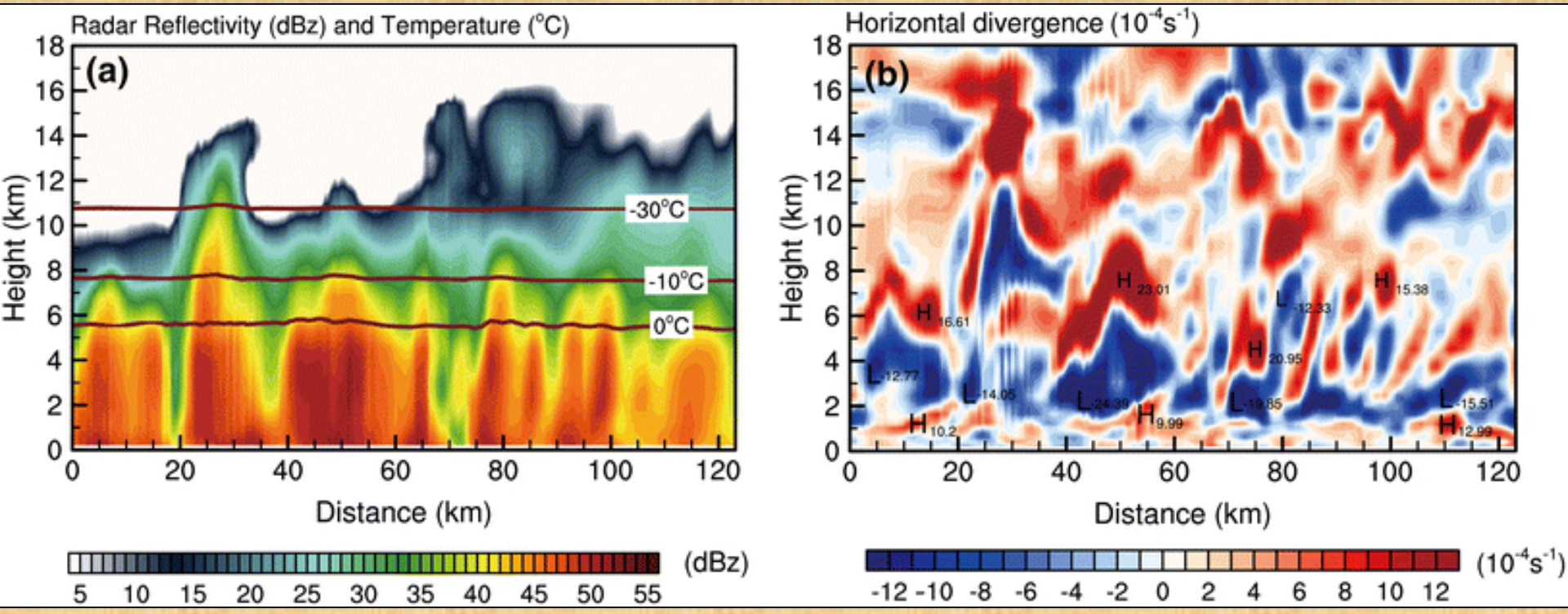

Fig. 7

Height-distance structures (clockwise) along the axis of the simulated SR, averaged radially within ±2 km of the axis.

Fig. 8

(a) The horizontal view of the SR2 axis and the radial cross sections (radially -30~60 km to the axis), also covering north segment of the SE (SE_{north}), downwind end of the PR1 ($PR1_{down}$) and downwind sector of the PR2 ($PR2_{down}$). **(b)** Model output reflectivity, θ_e, temperature and primary radius-height circulations (≥ 1 m s^{-1}). **The convection in the SR2 appears to be upright high-reflectivity tower surrounded by extensive stratiform precipitation (wave-like shallow precipitation and bright band structure).**

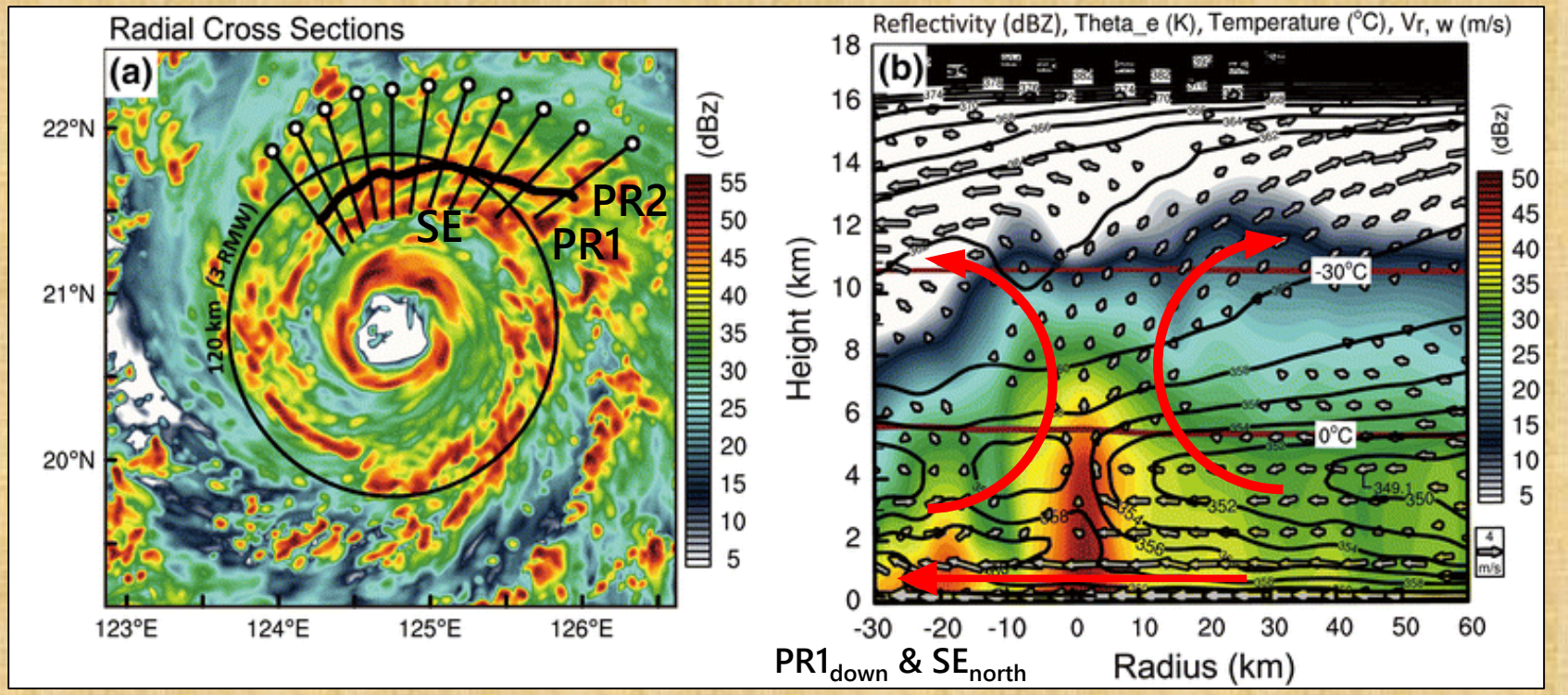

Fig. 8

(c) Radial wind of the SR2 with model output reflectivity [dBZ]. **Deep inflow (with an accelerated descending inflow channel) from outside was above the strongest inflow (> 20 m s^{-1}) within the BL. The BL inflow was blocked by eyewalls, decelerated and lifted (supergradient force), and then accelerated outward (subgradient force)** (Smith et al., 2009).

(d) Horizontal divergence.

(e) Vertical motion.

The encountering of inflow and outflow resulted in a major convergent core and formed a convective updraft tower. The updraft then turned outward and merged with the outflow of PE, or turned inward at 12–15 km height.

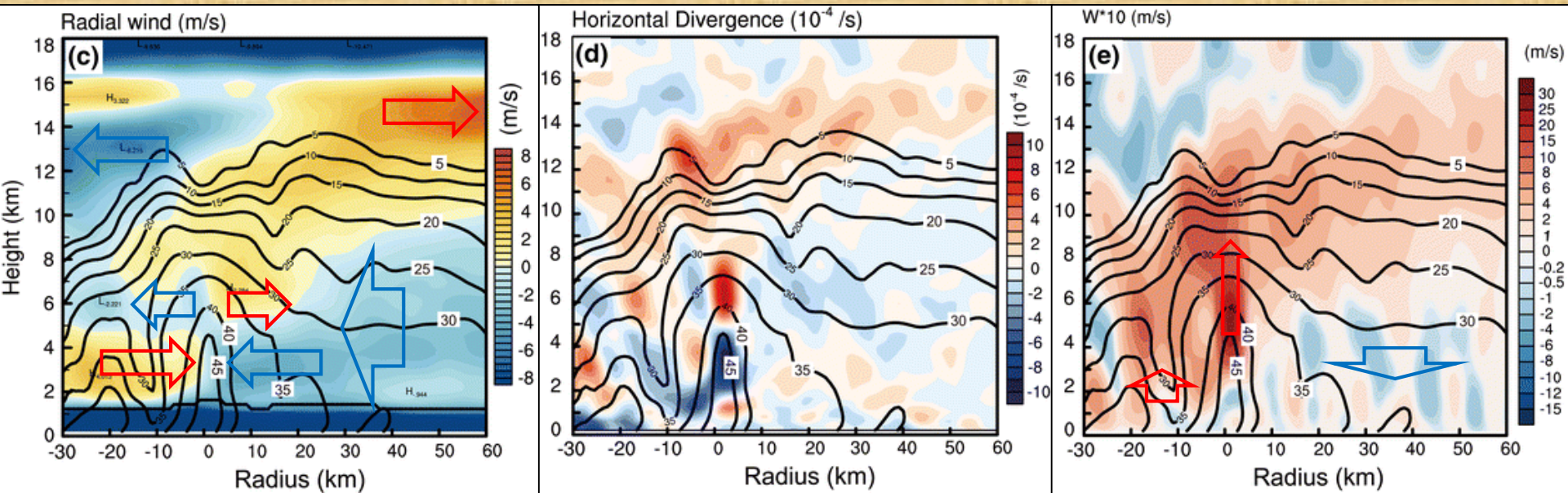

Fig. 8

(f) Angular momentum, saturated θ_e and primary radius-height circulations of the SR2.

The updraft tower was within convective instability (CI) layer as well as a conditional instability layer (not shown).

The slantwise descending and ascending motion were related to the conditional symmetric instability (CSI) at 1~2-km height, where $(slope)_{\theta_{se}} > (slope)_{M_g}$, indicating the release of baroclinic potential energy (Schultz and Schumacher, 1999).

 # CSN: convective symmetric neutral.

(g) Diabatic heating rate with model output reflectivity [dBZ].

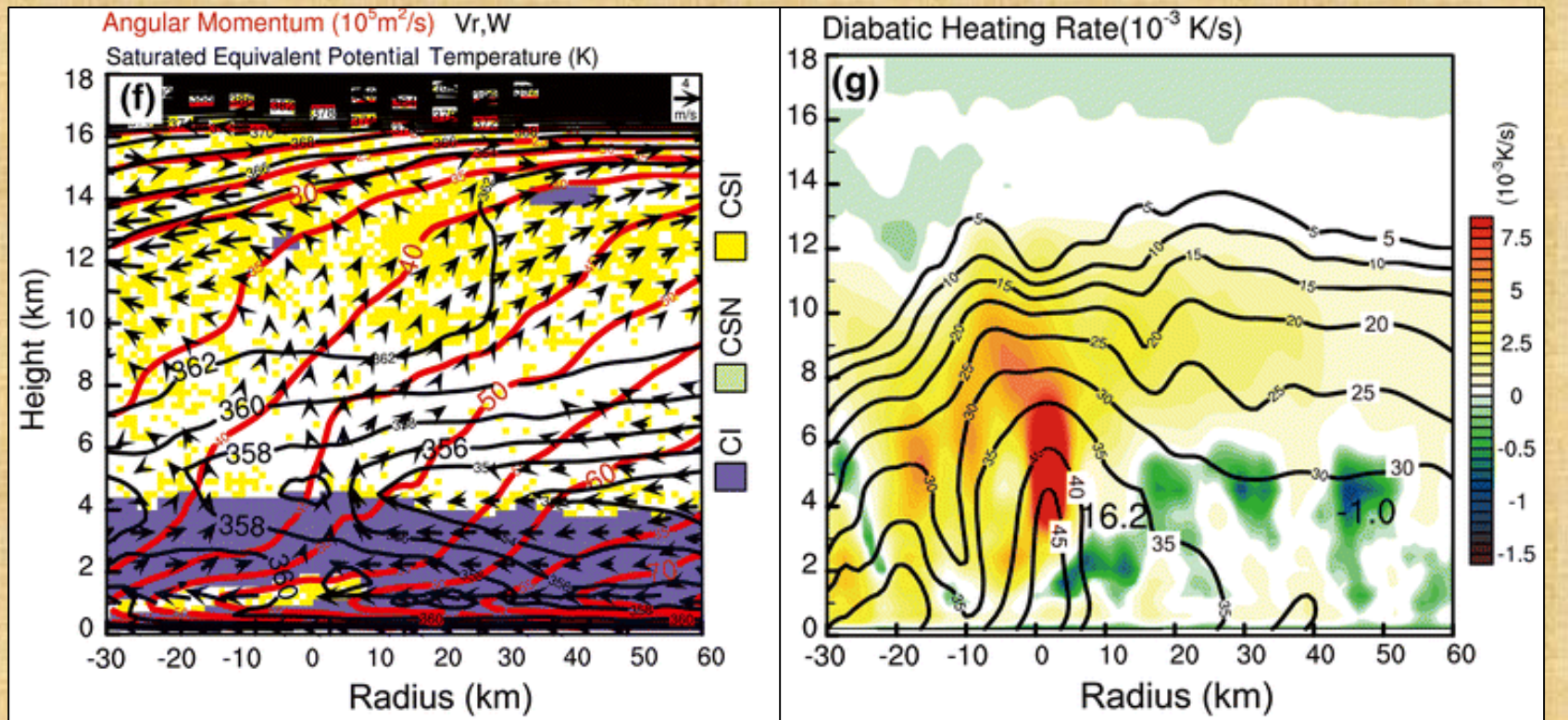

Fig. 8

(g) Diabatic heating rate with model output reflectivity [dBZ].

(h) Radial gradient of θ_e; **thin gray contours** are θ_e [K].

Large (negative) radial gradient of θ_e at the convergent region.

Latent heating (cooling) was also evident above (below) the melting level in the stratiform region, due to advection of θ_e, the radially decreasing in latent heating rate might further intensify the gradient of θ_e near the convection tower.

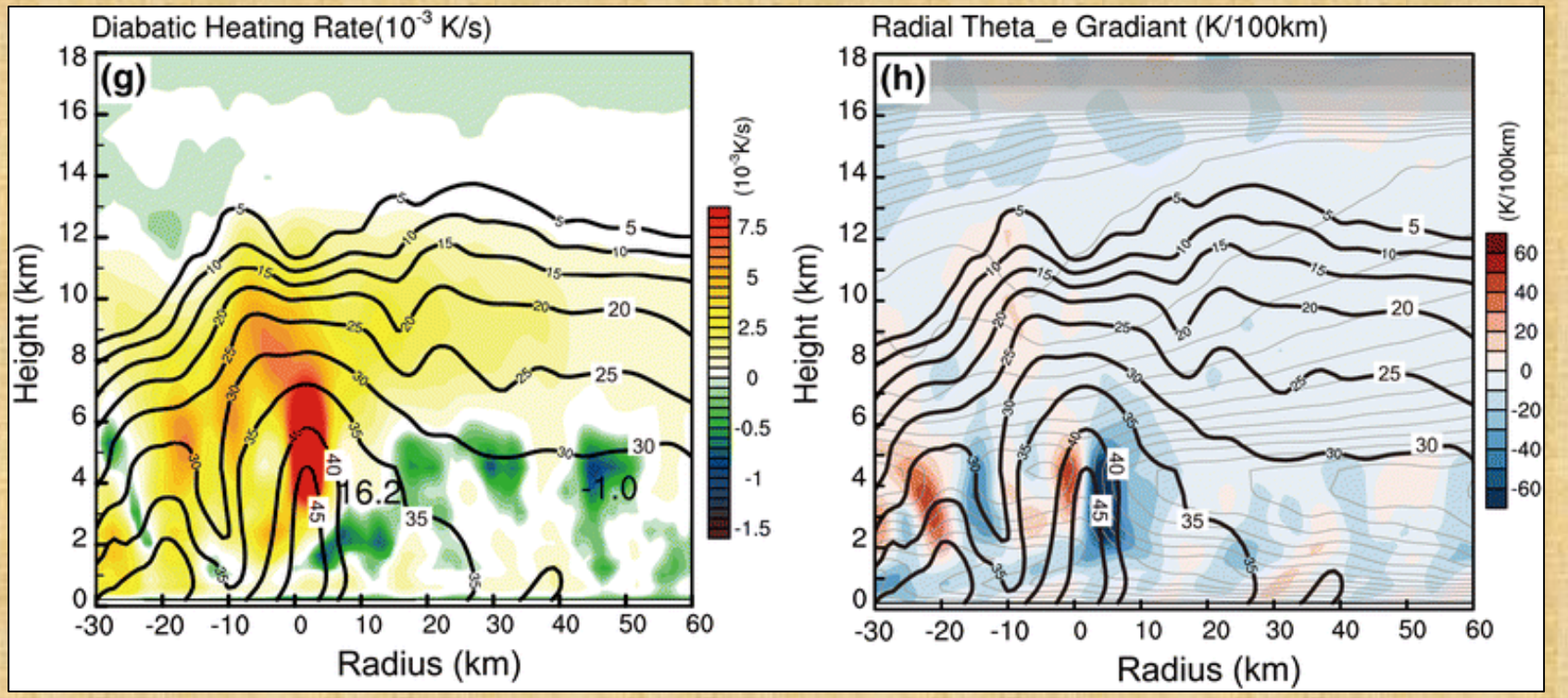

Fig. 8

(i) Tangential wind speed with model output reflectivity [dBZ].

(j) Radial anomaly of the asymmetric tangential winds (removing the radial mean at each vertical level).

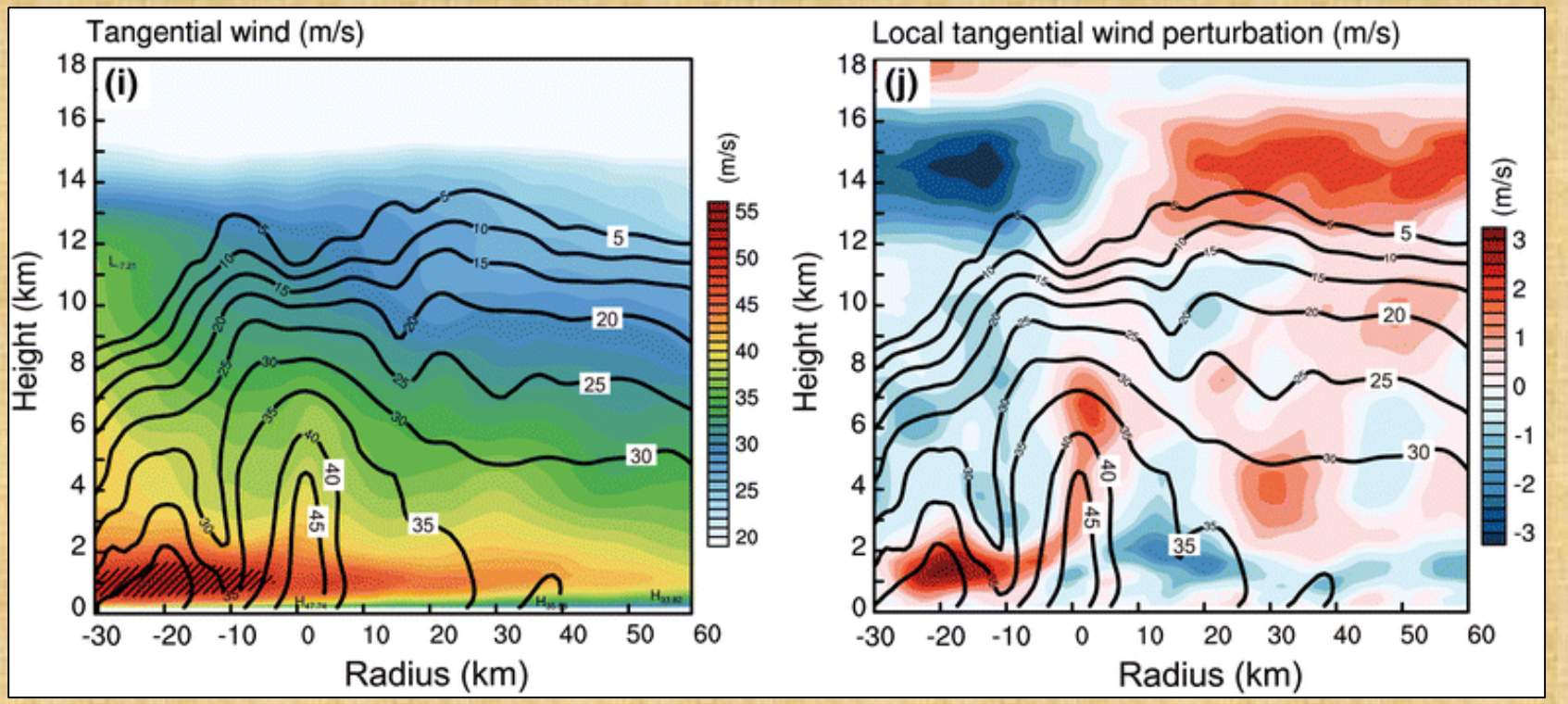

Tangential Wind Budgets

- $\frac{\partial v}{\partial t} = -u\eta - \frac{v}{r}\frac{\partial v}{\partial \lambda} - w\frac{\partial v}{\partial z} - \frac{1}{r\rho}\frac{\partial p}{\partial \lambda} + F_\lambda + BLF.$ (1)
- Left-hand side:
  Total tendency of tangential wind (v) component (VT_{TEND}).
- Right-hand side:
  Advection of… absolute vorticity (η) by radial wind (u) (RAD_{ADV});
  tangential wind by tangential wind (TAN_{ADV});
  tangential wind by vertical wind (w) (VER_{ADV});
  Horizontal pressure (p) gradient force (P_{GRD});
  Diffusion (DIFF);
  Boundary layer friction (BLF).
- DIFF is much smaller except near the eyewall (Wang, 2002b; Yau et al., 2004).
  As a reference, the tangential wind difference was obtained by subtracting V_t at 6 min earlier.

Wind components excludes the movement of the TC.

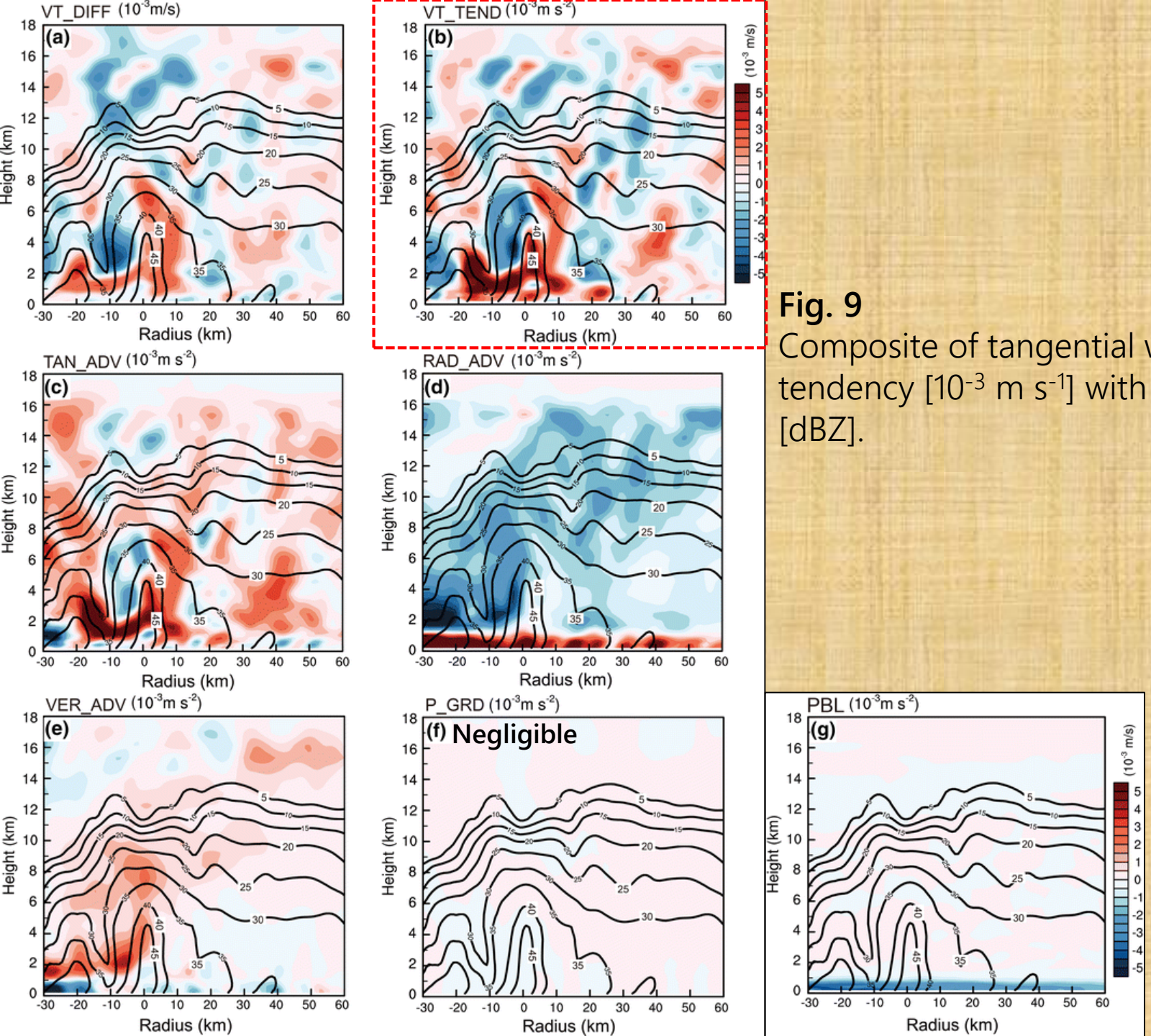

Fig. 9
Composite of tangential wind (V_t) tendency [10^{-3} m s^{-1}] with reflectivity [dBZ].

Comparison with Secondary Rainbands in Previous Studies

- **Hurricane *Rita* (2005) (**Didlake and Houze, 2013a**).**

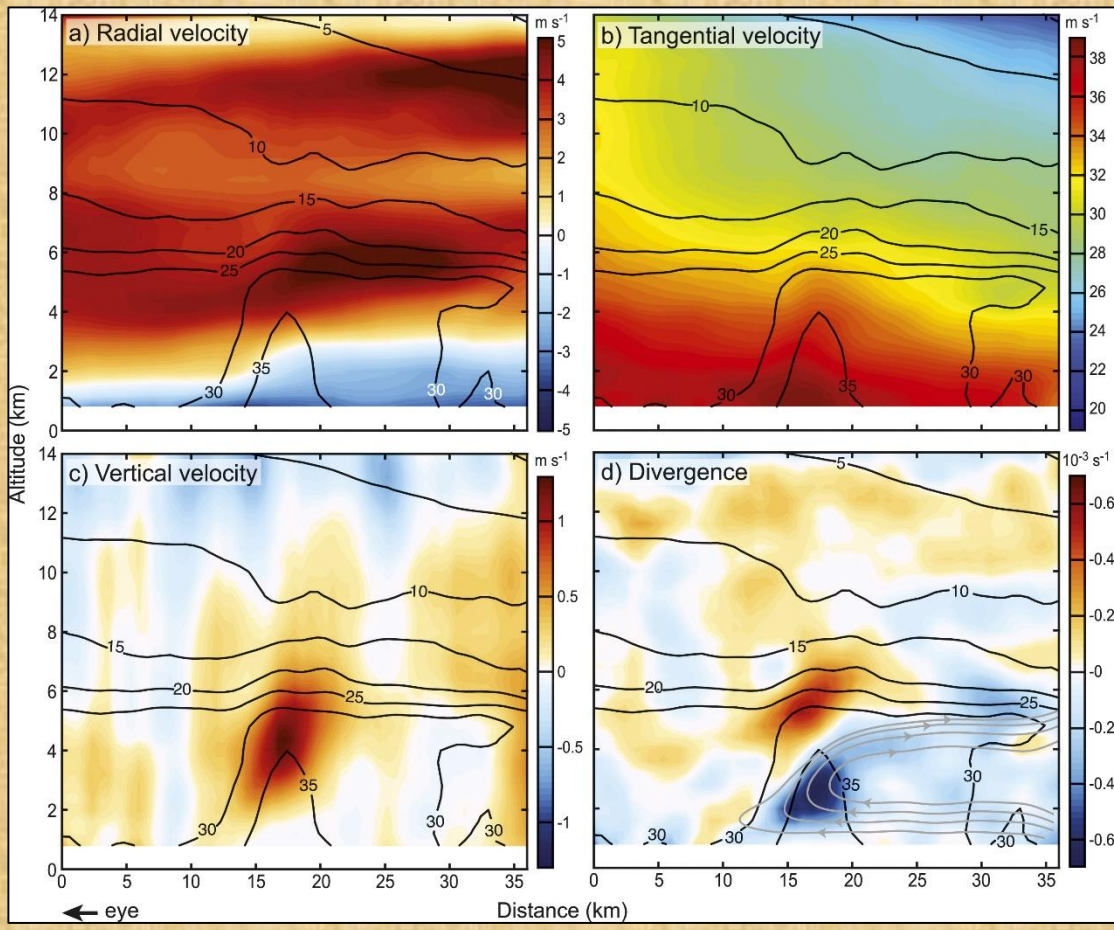

Fig. 3 Composite radius-height structures of convective cells in the inner upwind region of *Rita*.

Comparison with Simulated Principle Rainbands in Jangmi

Reflectivity, θ_e, temperature and primary radius-height circulations.
Left (Fig. 10a): PR1_mid.
Right (Fig. 8b): SR2.

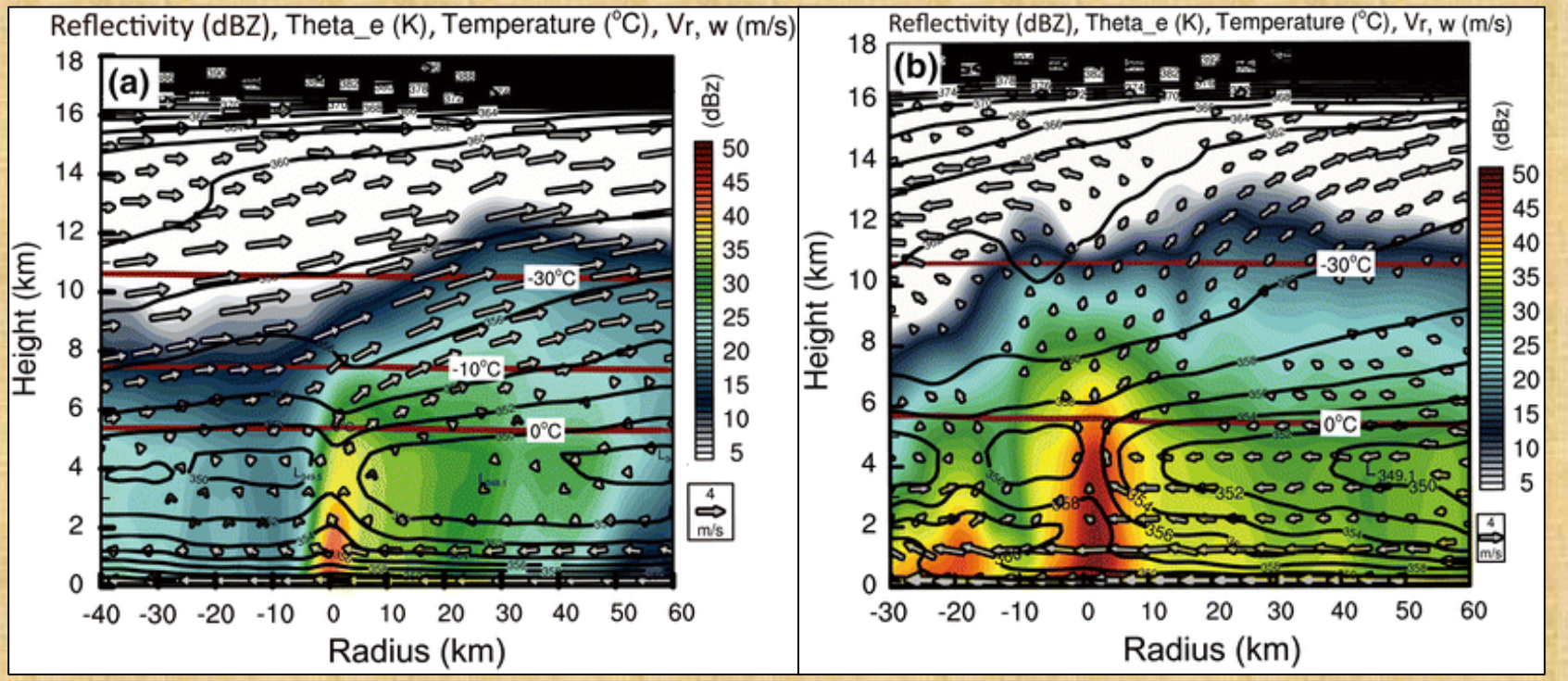

Comparison with Simulated Principle Rainbands in Jangmi

Horizontal divergence.
Left (Fig. 10b): PR1_mid.
Right (Fig. 8d): SR2.

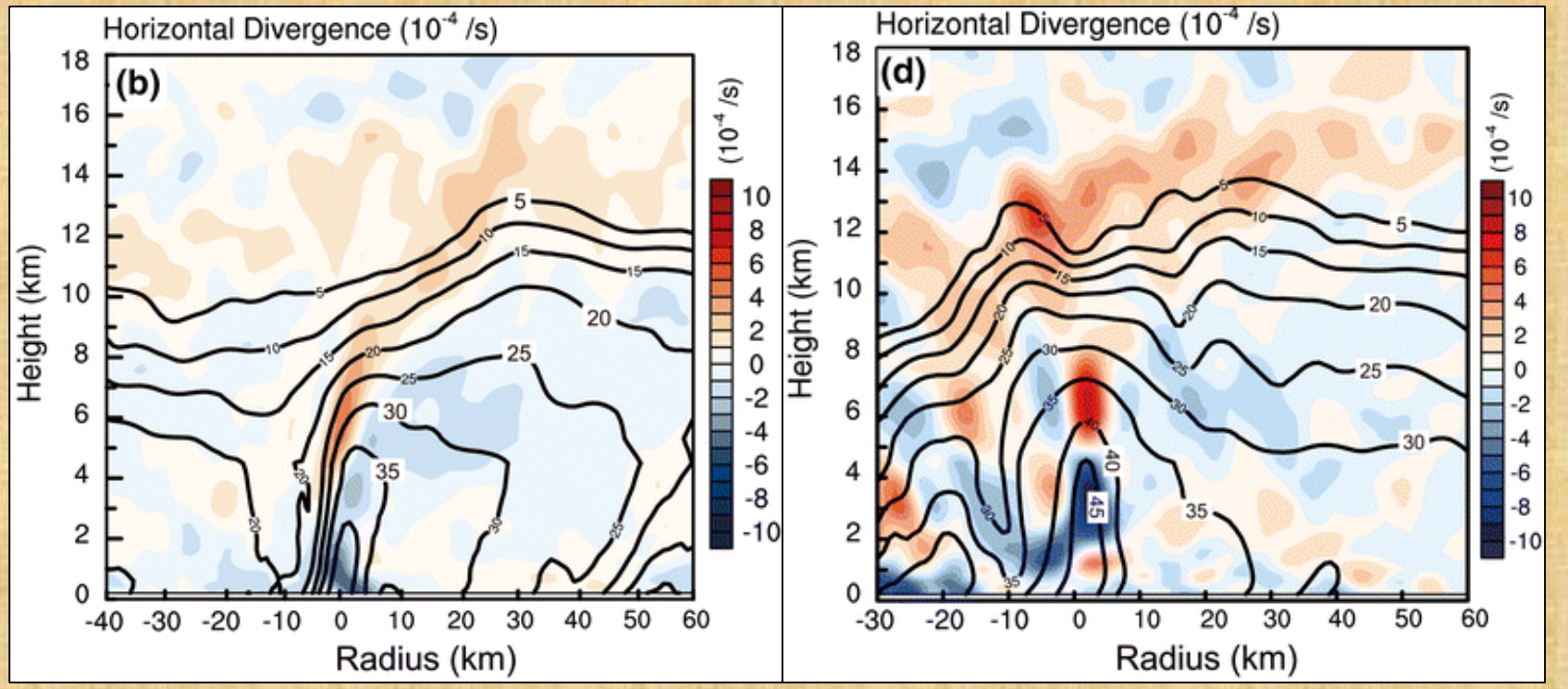

Comparison with Simulated Principle Rainbands in Jangmi

Vertical velocity.
Left (Fig. 10c): PR1_mid.
Right (Fig. 8e): SR2.

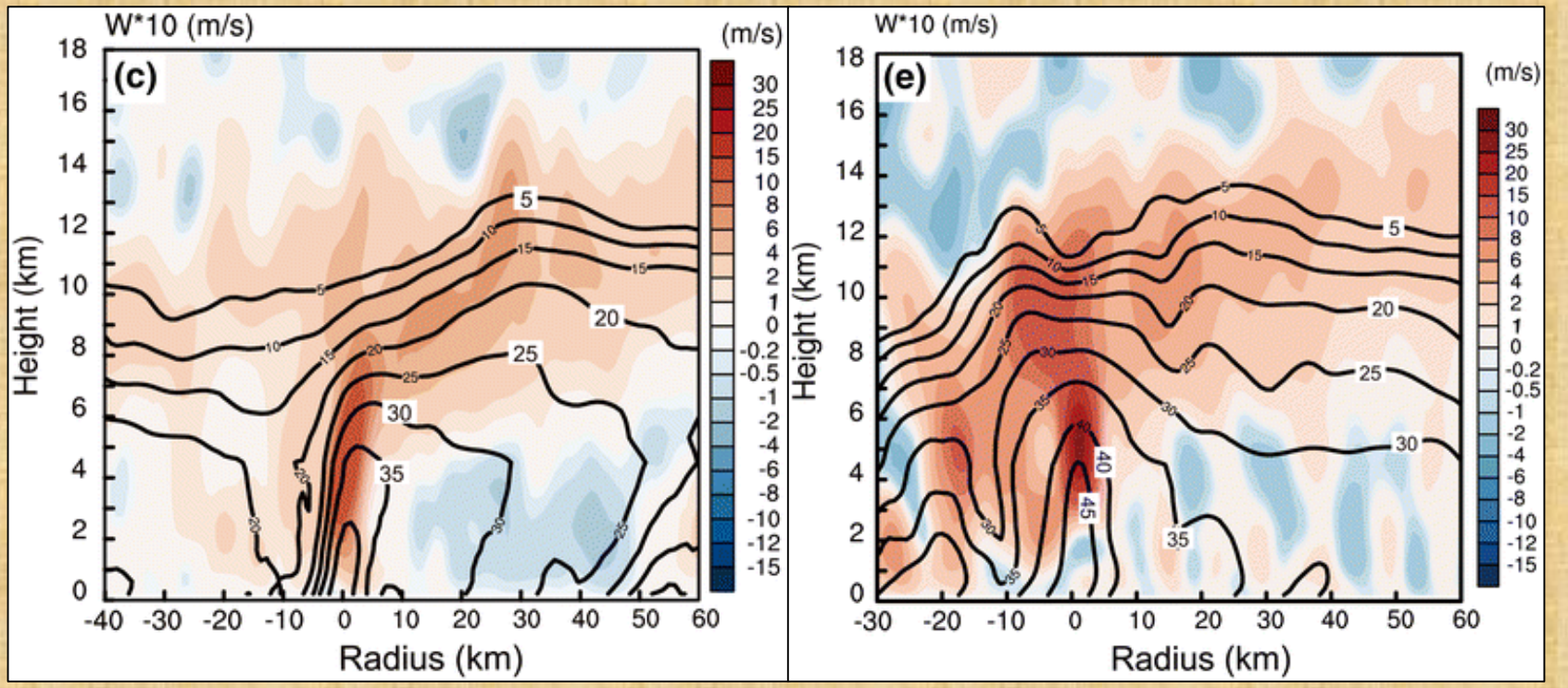

Comparison with Simulated Principle Rainbands in Jangmi

Local tangential wind perturbation.
Left (Fig. 10d): PR1_mid.
Right (Fig. 8j): SR2.

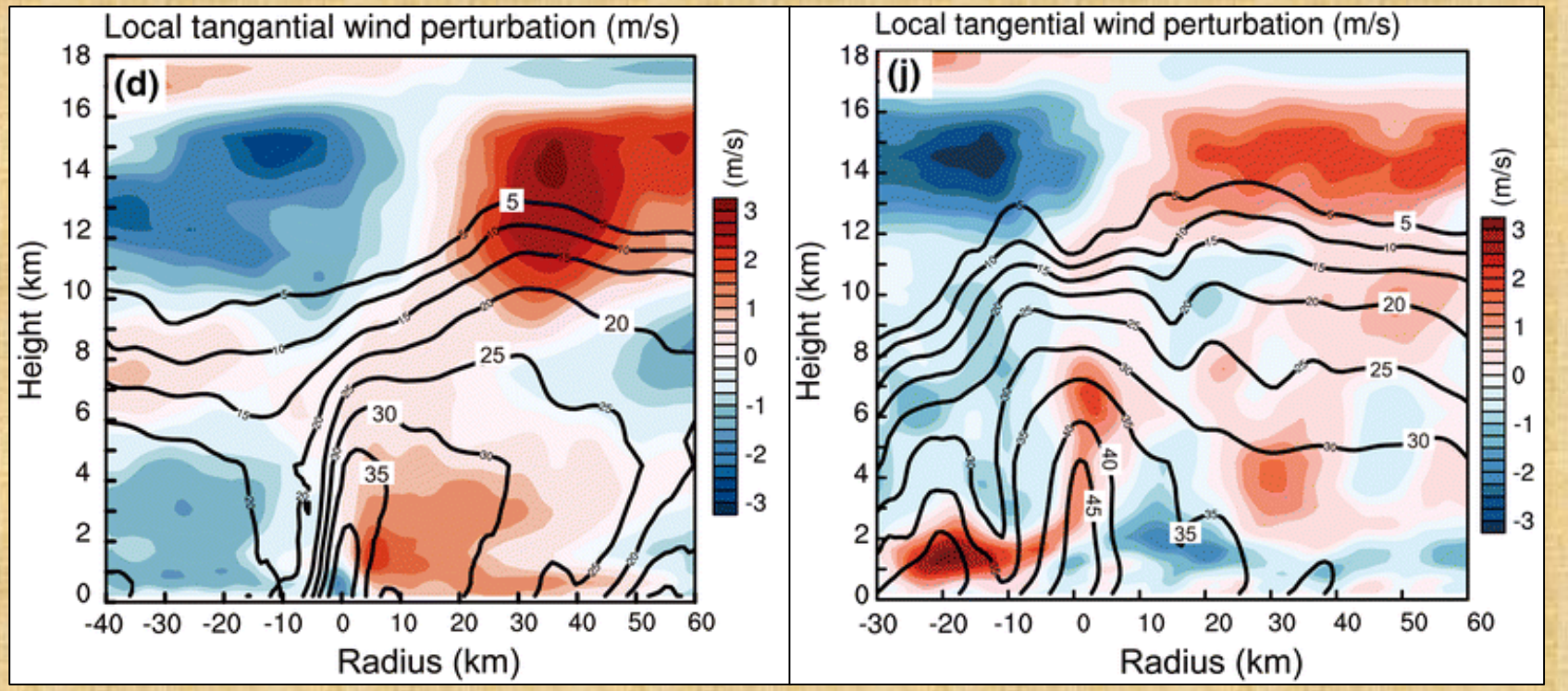

Fig. 15
Variation of contoured frequency with radius in rainbands.

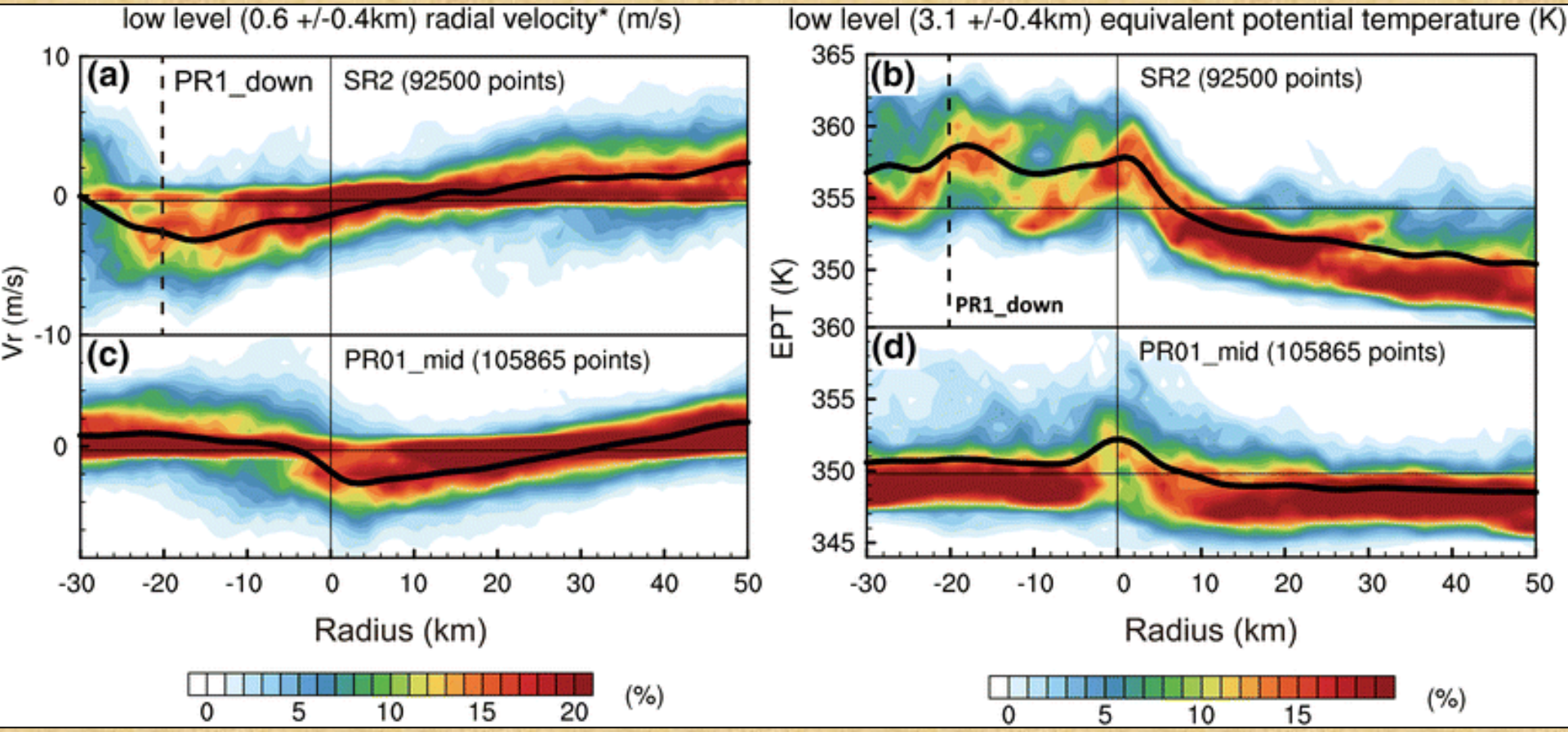

Comparison with Simulated Principle Rainbands in Jangmi

Reflectivity, θ_e, temperature and primary radius-height circulations.
Lower left (Fig. 11a): PR1_down.
Lower middle (Fig. 10a): PR1_mid.
Lower right (Fig. 11c): PR1_up.
Upper right (Fig. 8b): SR2.

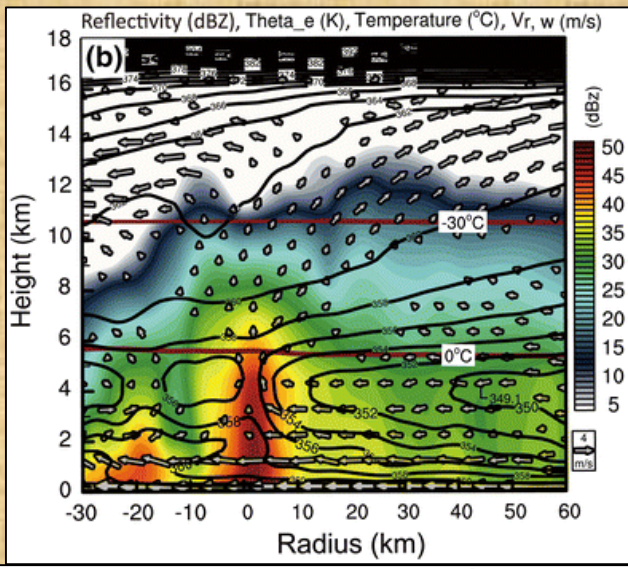

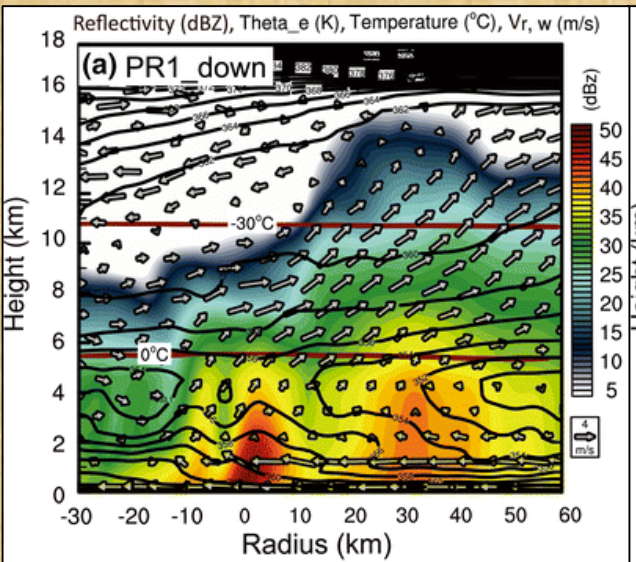

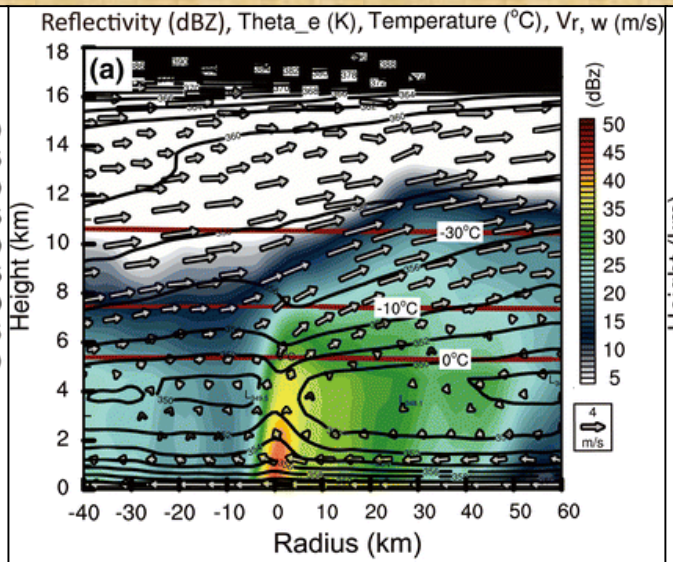

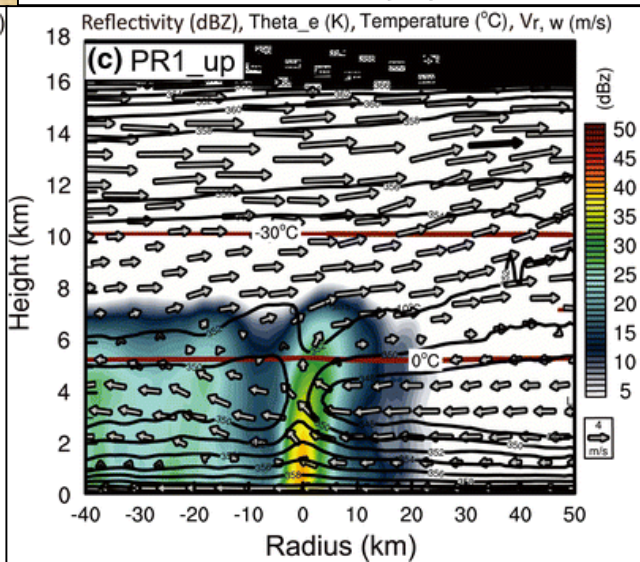

Comparison with Simulated Principle Rainbands in Jangmi

Horizontal divergence.
Lower left (Fig. 11b): PR1_down.
Lower middle (Fig. 10b): PR1_mid.
Lower right (Fig. 11d): PR1_up.
Upper right (Fig. 8d): SR2.

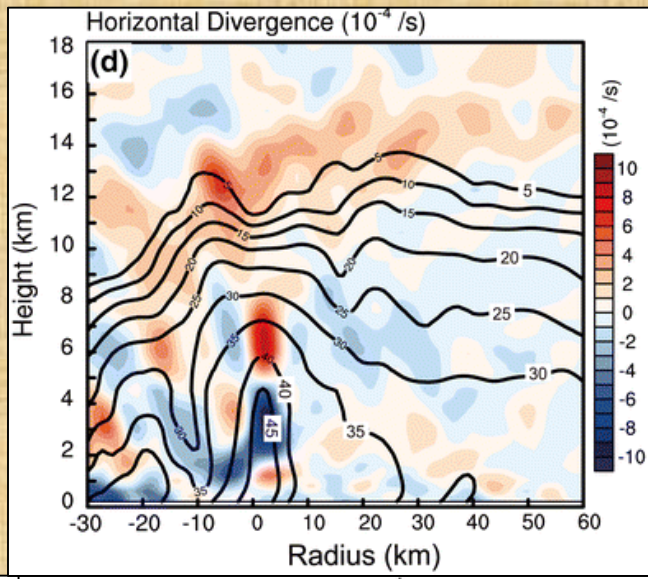

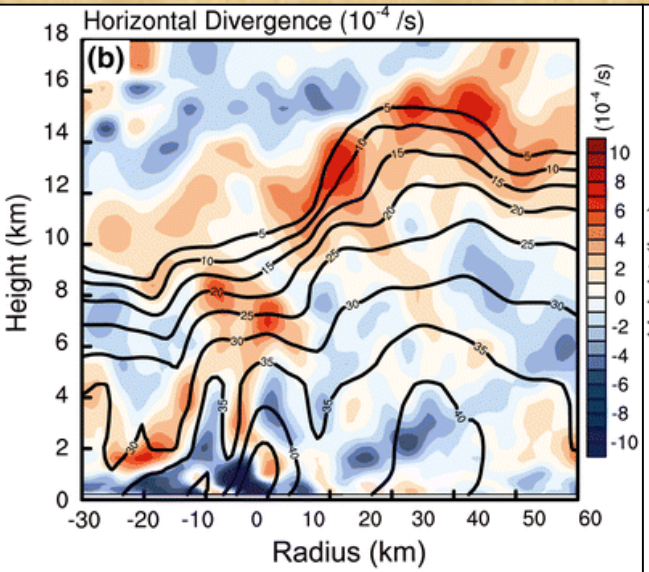

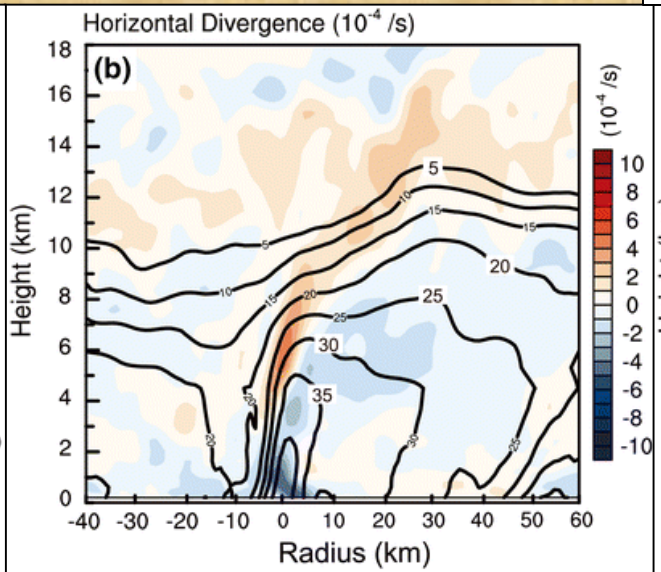

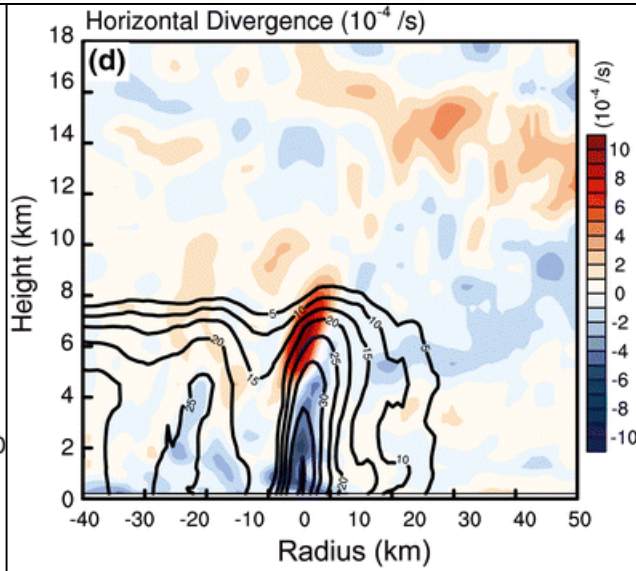

IV)
Formation and Evolution of Convection in Secondary Rainbands

Evolution of the Convections

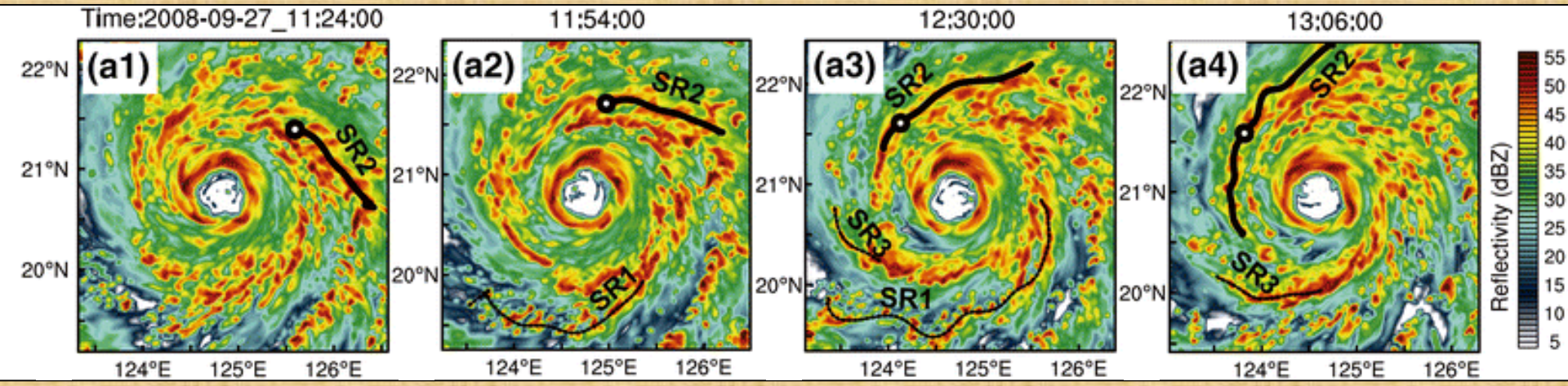

Fig. 12a
Evolution of SR2, horizontal view.
1–4: 71.4, 71.9, 72.5 and 73.1 h.

Fig. 12b–d Evolution of SR2.
1–4: 71.4, 71.9, 72.5 and 73.1 h.

Developing stage

Decaying stage

Reflectivity with θ_e and circulations

Radial wind with reflectivity

Divergence with reflectivity

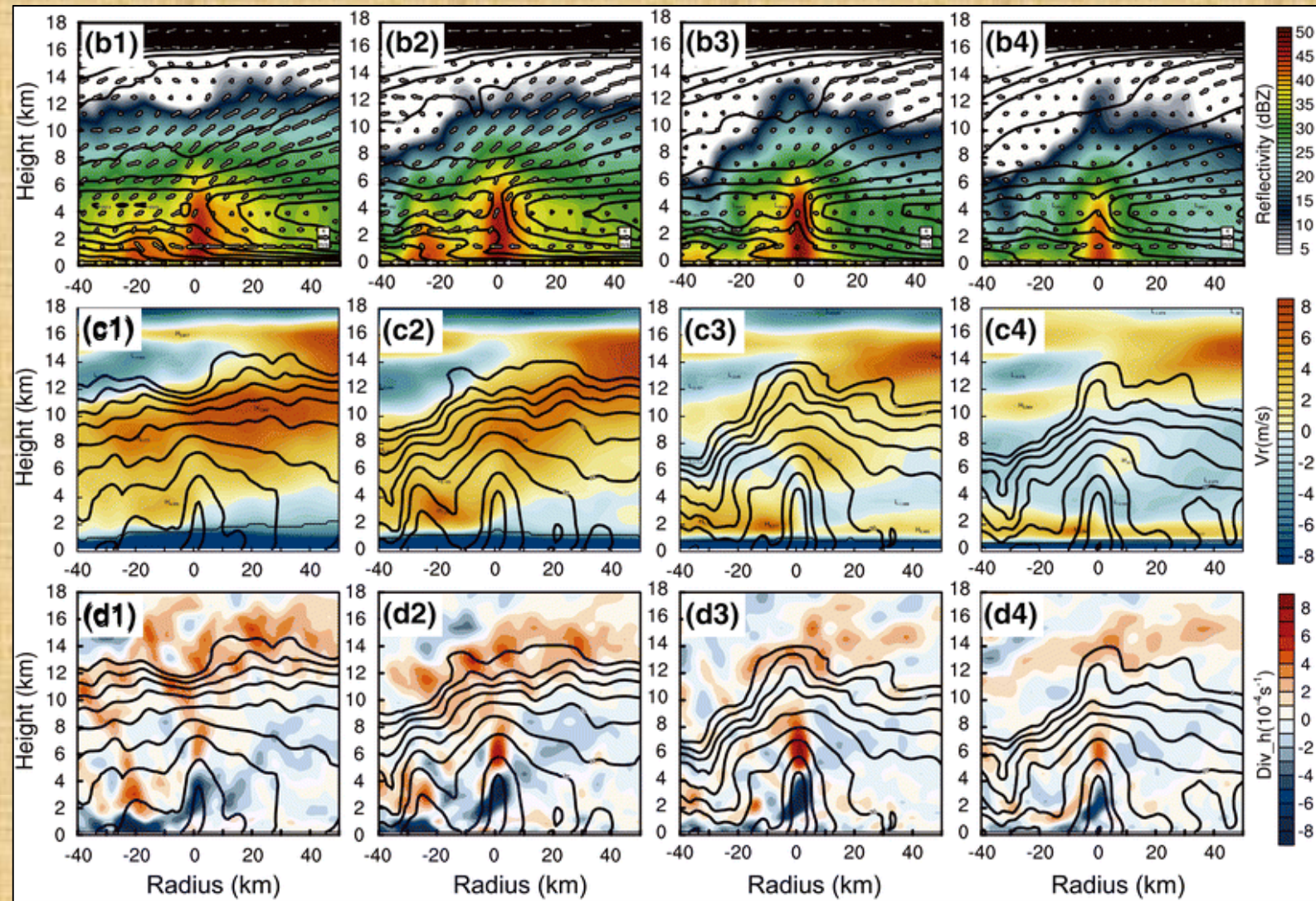

Evolution of the Convections

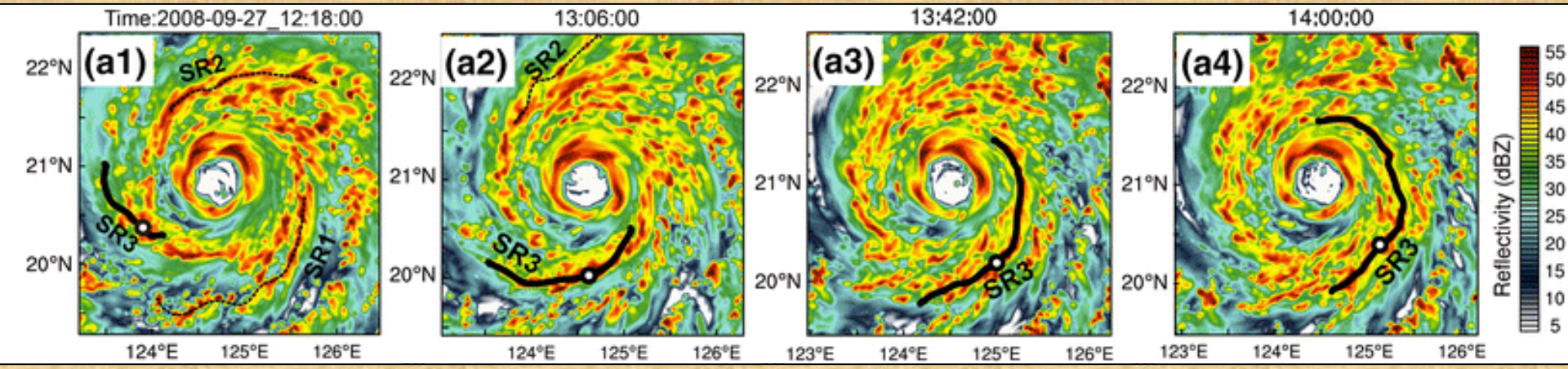

Fig. 13a
Evolution of SR3, horizontal view.
1–4: 72.3, 73.1, 73.7 and 74.0 h.

Fig. 13b–d Evolution of SR3;
1–4: 72.3, 73.1, 73.7 and 74.0 h.

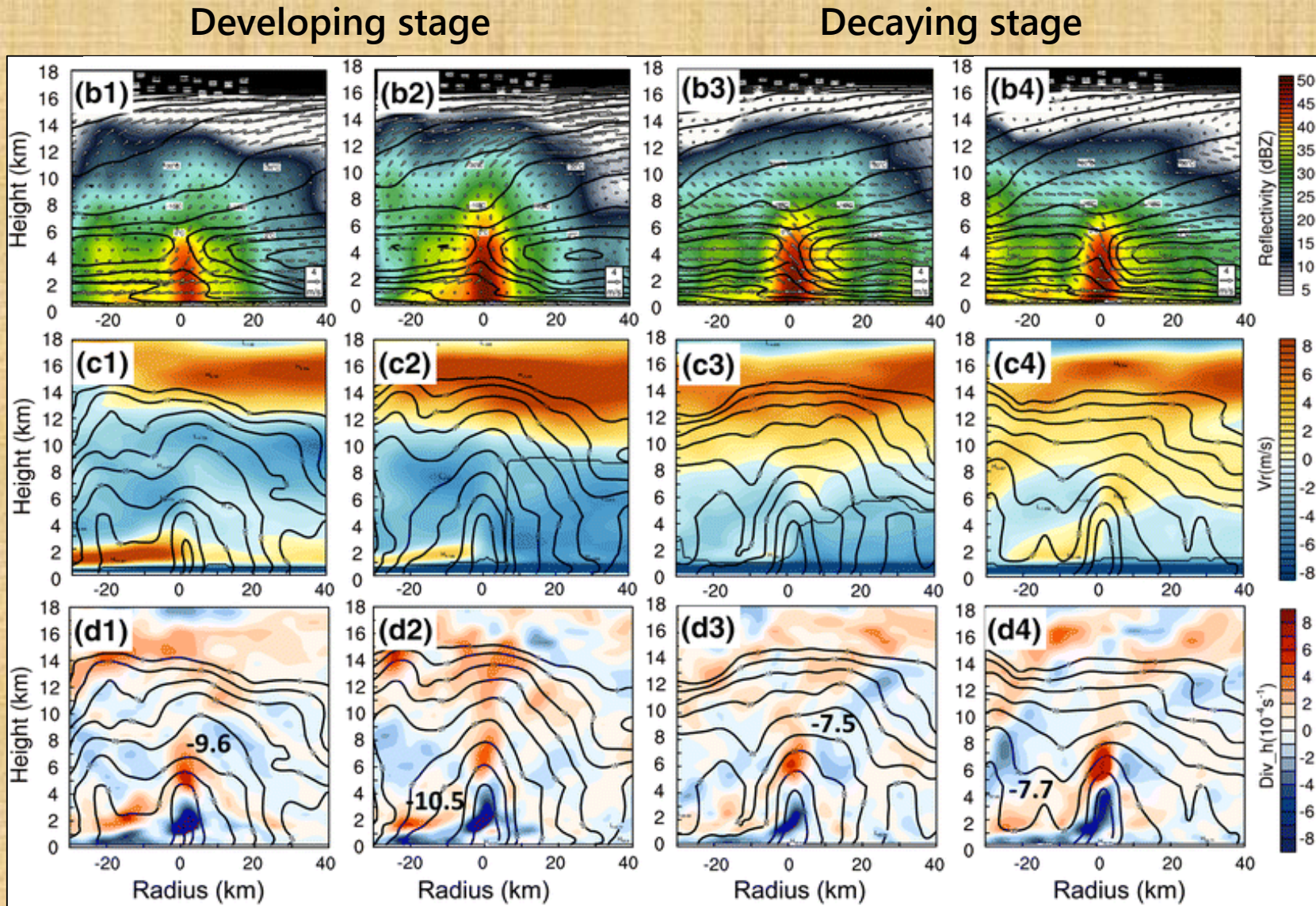

Evolution of the Convections

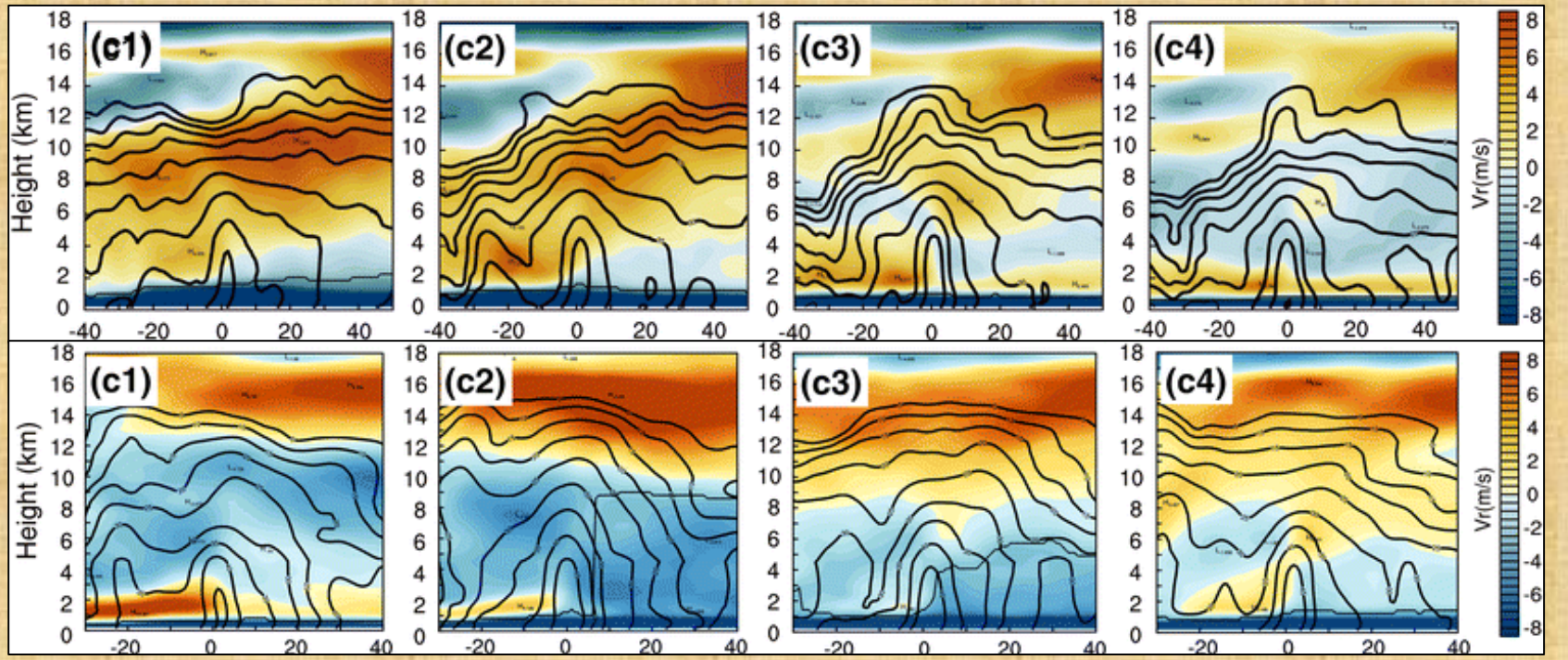

The major difference between SR2 (Fig. 12c) and SR3 (Fig. 13c) is the evolution of radial wind fields due to the difference in the vertical wind shear in the NNW direction.

Three-Dimensional Trajectories

- Three-dimensional trajectories were calculated to verify the formation of SRs convection.
- The model output data at 6 min interval were interpolated to data with a temporal resolution of 5 s.
- Only parcels at those cross-sections with $w > 0.5$ m s^{-1} (updraft center) at 5-km height above the rainband axis were chosen.

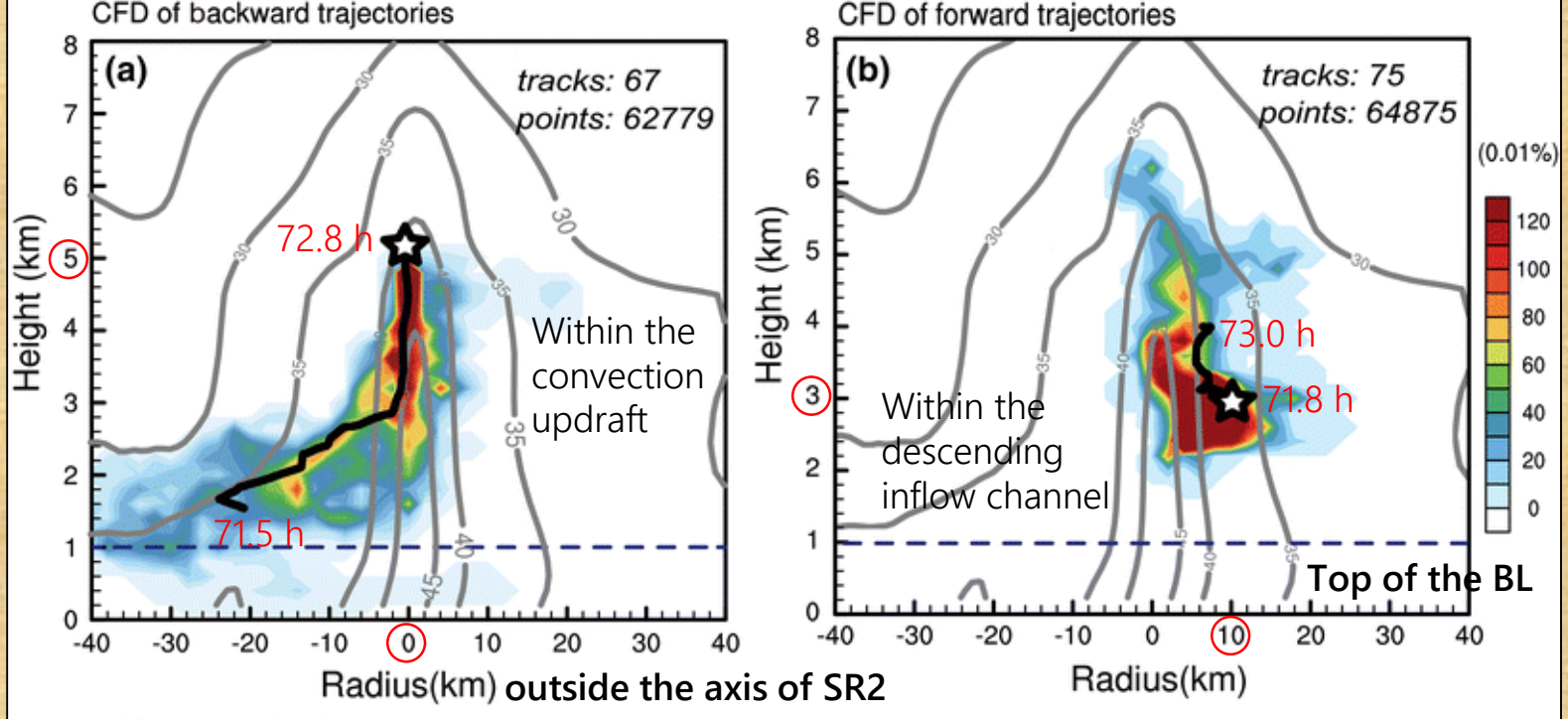

outside the axis of SR2

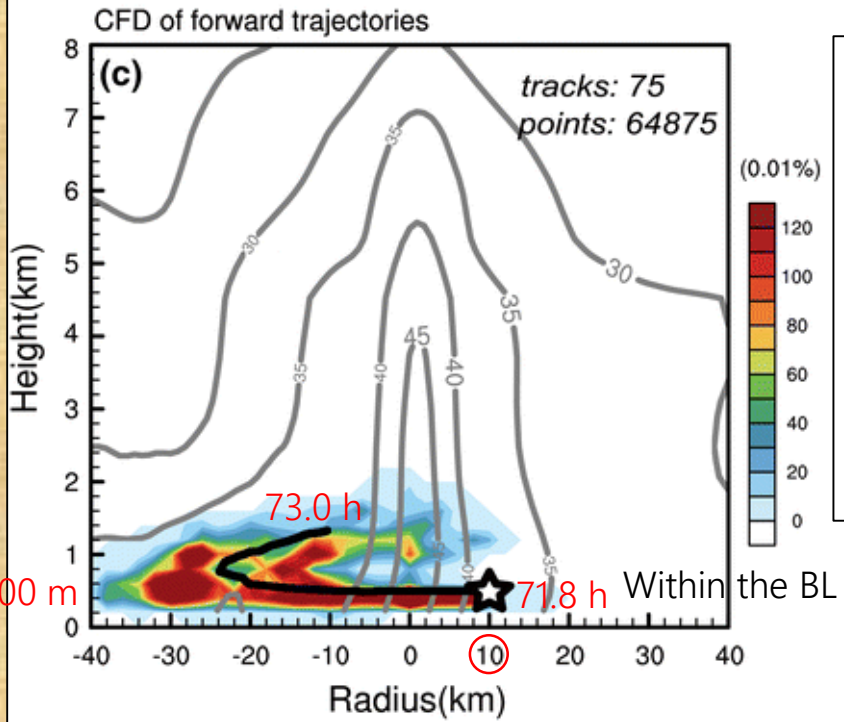

Fig. 14
Contoured frequency diagrams (CFDs) of **(a)** backward trajectories, **(b)(c)** forward trajectories.
 # Gray contours: 71.5–73.0 averaged reflectivity [dBZ];
Thick black lines: averaged trajectories.
Stars: first locations of tracer points.

Three-Dimensional Trajectories

- **The results confirms that convections in the SRs are triggered above the BL, similar to the kind of "elevated convection" in previous studies (Colman, 1990a, b; Horgan et al., 2007; Corfidi et al., 2008).**
- **An "elevated convection" is usually associated with a gently sloping warm front above a cold and stable BL (Moore et al., 2003).**

V)
Discussions

Are Secondary Rainbands Equivalent to the Inner Rainbands?

- In some idealized simulations such as Li and Wang (2012b), the structures of the inner rainbands were essentially equivalent to the SRs in this study, but how the convergent flow was formed in the first place remains uncertain.
- In the real-case study by Moon and Nolan (2015a, b), the SR was similar to the PR, while the inner rainband had different characteristics:

1. The high-reflectivity core extended to 5-km height only.
2. The ascending motion was initiated above 2-km height at the outer edge of the reflectivity core, while the descending motion was located at the inner edge and down to the surface.
3. A slantwise strip of high cloud mixing ratio can be found around 1-km height inside the high-reflectivity core, with higher θ_e, lower radial inflow and higher tangential wind.

Possible Impacts on TC's Structure

- **Because of the release of CSI, SRs may accelerate the BL inflow, resulting in tangential wind increments near the top of the BL in the inner side due to the super-gradient force and friction (Smith et al., 2009; Qiu and Tan, 2013; Wang et al., 2013).**
- **The tangential wind increment is favorable to the formation of a strong convergence ring and may intensify the SE (Huang et al., 2012).**
- **The latent heat generated by the inner ascending motion and the diabatic cooling due to the outer descending motion may further amplify the θ_e gradient and the cross-front secondary circulation.**
- **The effects of SRs on the structure and intensity of a TC, and their interactions with SEs still need to be further studied.**

VI)
Summary

Summary

- Investigated the secondary rainbands (SRs) of *Jangmi* (2008) by a cloud-resolving scale numerical simulation.
- Tracked the axes of the rainbands by semi-automatic rainband tracking algorithm.

Summary

- Slantwise-vertical ascending motion in the lower to middle layer: CSI region at 1–2 km height is baroclinic due to the convergence of warmer (inner) and colder (outer) air; CI region at 2–5 km height may enhance the vertical convection.
- Penetrating descending inflow may accelerate the boundary inflow inside the axis, facilitating the formation or intensification of the SE.
- Latent heating and cooling may further amplify the potential temperature contrast and the cross-front secondary circulation.

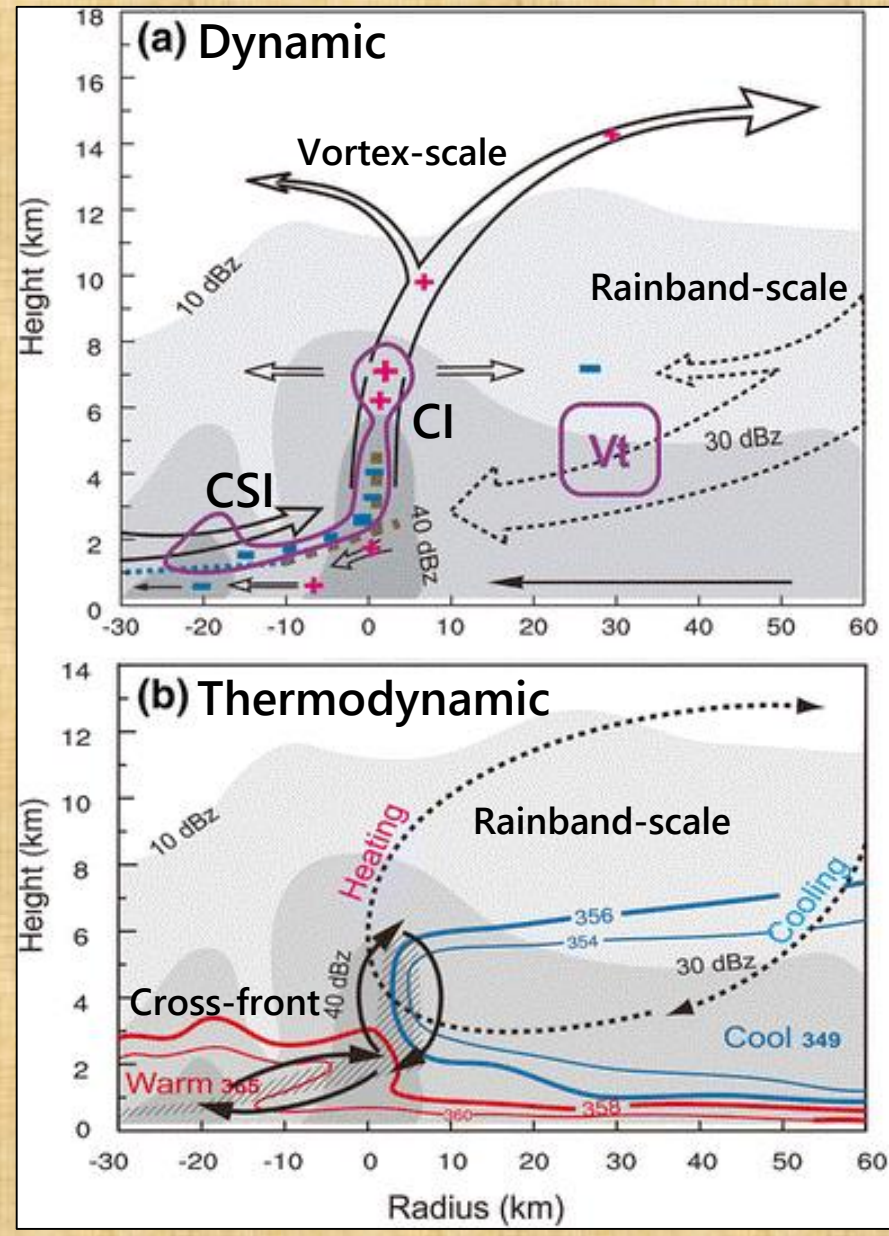

Fig. 16 Schematic diagrams of the structures of the SRs in *Jangmi* (2008).

Summary

- Local tangential wind maxima (encompassed by purple lines) in the slantwise-vertical ascending region is contributed by vertical advection with the tangential wind budget analysis.
- SR convection has the major source of air in the above-boundary outflow layer inside the convection core with 3D forward and backward trajectories.

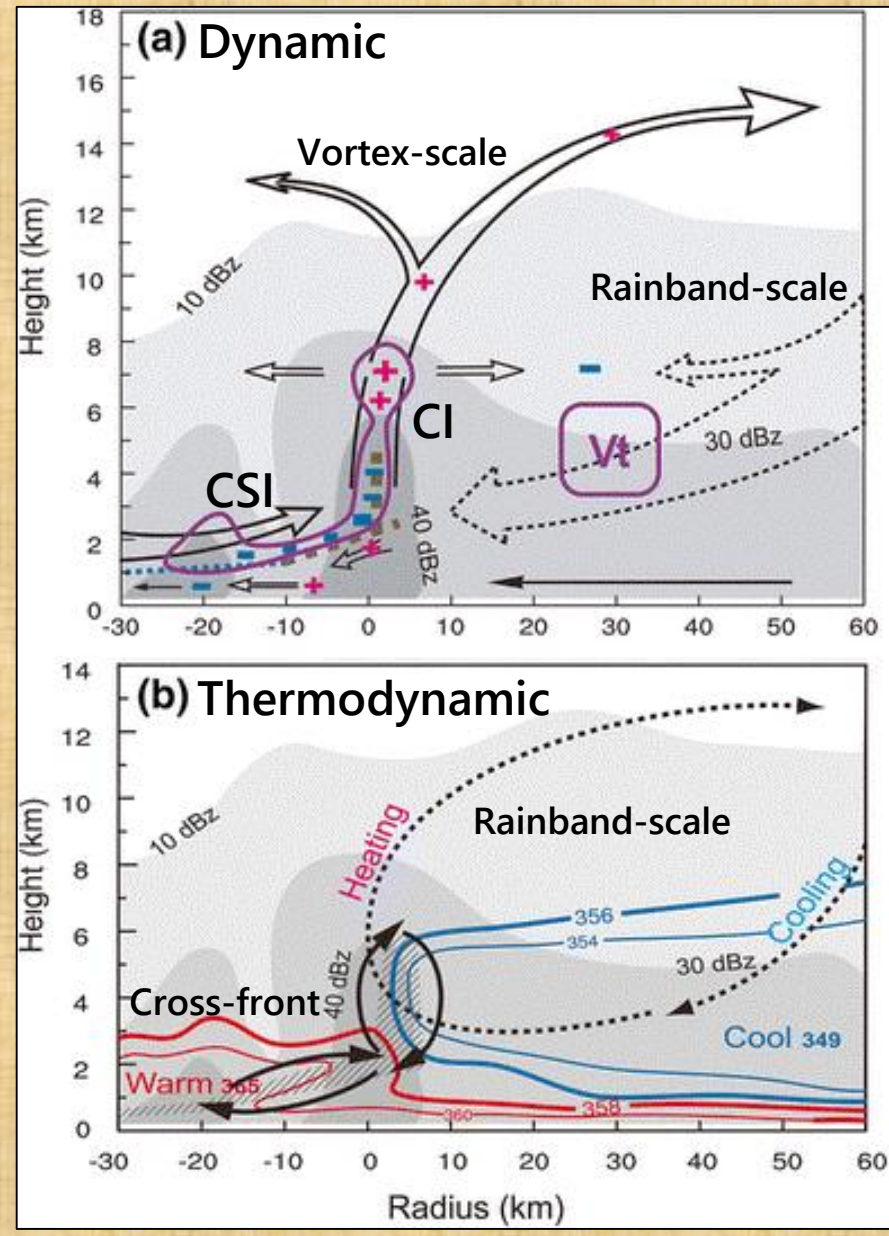

Fig. 16 Schematic diagrams of the structures of the SRs in *Jangmi* (2008).

Summary

Table 2 The differences between secondary rainbands (SR) and mid-wind sector of principal rainbands (PR_mid)

	SR	PR_mid
Trigger mechanism	Above-boundary layer convergence between mid-level descending inflow and above-boundary layer outflow	Within boundary layer blocking of the radial inflow
Instability	CSI (1~2-km height)—CI (2~4.5-km height)	CI (start from the boundary layer)
Updraft motion	slantwise (1~2-km height)—upright (2.5~8-km height)	nearly upright (below 8 km height)
Descending motion	panetrates the bottom of the convection and accelerates the boundary layer inflow	are blocked by the convection cores or descending around them
V_t increment	Within slantwise and upright rising region, which can intrude into the boundary layer inside the convection core.	around the boundary layer top and limited on the outer edge of the convection core
Cross-band V_r	accelerates inward in boundary layer	decelerates inward
Cross-band θ_e	rapidly rising inward between 2~4-km height	no obvious differences

V_t, V_r, θ_e denote the tangential, radial wind component and the equivalent potential temperature, respectively; CSI and CI are the conditional symmetric and convective instability

References

- Didlake, A.C. & Houze, R.Z. (2013a). Convective-scale variations in the inner-core rainbands of a tropical cyclone. *J. Atmos. Sci.* **70**, 504–523.
- Smith, R. K., Montgomery, M. T. & Vogl, S. (2008). A critique of Emanuel's hurricane model and potential intensity theory. *Q. J. R. Meteorol. Soc.* **134(632)**, 551–561.
- Spencer, R.W., Goodman, H.M., Hood, R.E. (1989). Precipitation retrieval over land and ocean with the SSM/I: Identification and characteristics of the scattering signal. *J. Atmospheric Ocean. Technol.* **6(2)**, 254–273.

The End